

DEPENDENCE OF THE PREDICTED PAIR-INSTABILITY SUPERNOVA RATE
ON THE POP III INITIAL MASS FUNCTION

by

ALESSA IBRAHIM WIGGINS

Bachelor of Arts, 2019
California State University San Bernardino
San Bernardino, CA

Submitted to the Graduate Faculty of the
College of Science and Engineering
Texas Christian University
in partial fulfillment of the requirements
for the degree of

Master of Science

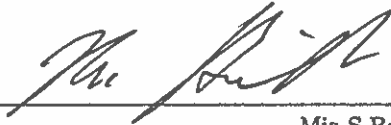
December 2021

DEPENDENCE OF THE PREDICTED PAIR-INSTABILITY SUPERNOVA RATE
ON THE POP III INITIAL MASS FUNCTION

by

Alessa Ibrahim Wiggins

Dissertation Approved:



Mia S Bovill



Peter M Frinchaboy III



Kat Barger



Hana Dobrovolny



Massimo Stiavelli



For The College of Science and Engineering

Copyright by
Alessa Ibrahim Wiggins
2021

ACKNOWLEDGEMENTS

I would like to express my sincere gratitude to my advisor Dr. Mia Sauda Bovill for her support and guidance in preparation of this work.

I would like to thank the members of my thesis committee, Dr. Peter Frinchaboy, Dr. Kat Barger, Dr. Hana Dobrovlny, and Dr. Massimo Stiavelli for their mentorship.

Special thanks to my parents, Wissam and Ghedaa, for supporting me throughout my entire life, and my sisters for believing in me. I would also like to thank my amazing fiancé, Lucas, for being there for me every hour of every day.

Finally, I would like to thank my spiritual mentor, Hussam, for introducing me to Astronomy at a very young age, and for always believing in me.

Contents

1	Introduction	1
1.1	The formation of structure	1
1.2	The first stars	3
1.3	Fates of Pop III Stars	6
1.3.1	Core Collapse Supernova	6
1.3.2	Pair Instability Supernova	7
1.3.3	Direct Collapse Blackhole	7
1.4	Detection of the first stars	9
2	Simulations	11
2.1	AMIGA Halo Finders	13
2.2	Merger Trees	14
2.3	Semi Analytic Model	15
2.3.1	Lyman-Werner Background	15
2.3.2	Metal Enrichment	17
3	Modeling the Pair Instability Supernovae Rate	21
3.1	Pop III IMF	22
3.1.1	How is our model populating the IMF?	24
3.2	Random population of the IMF	26
4	Results	28
4.1	PISN Rate Calculations	30
4.1.1	Effect of the Maximum Pop III Mass	37
5	Discussion and Conclusion	44
5.1	Discussion	44
5.2	Conclusions	46
6	Future Work	48
A	PISN Rate Calculations	50
	Vita	
	Abstract	

List of Figures

1.1	The mass of a dark matter halo as a function of cosmological redshift. (M. S. Bovill, private communication)	3
1.2	The cooling function for stars with different metallicities.	6
1.3	Final mass vs initial mass function of non-rotating primordial, Pop III stars ($Z = 0$) from Heger & Woosley (2002) with modifications.	8
1.4	Stars metallicity as a function of their initial masses.	10
2.1	Flow chart of the steps we use to model the first stars, with the goal of making predictions for JWST.	12
2.2	Halo mass function at different redshifts. This plot shows the number of halos per dark matter virial mass $\left(\frac{dN}{dM_{vir}}\right)$ at redshifts $z = 6, 10, 20$, respectively.	14
2.3	The two cases of the Lyman-Werner backgrounds used in our SAM plotted as a function of redshift. These figures are taken from Figures 2 and 7 from Trenti & Stiavelli (2009), respectively. The left figure represents the low LW background (red curve in Figure 2.4), and the right figure is for a high LW background (gold curve in Figure 2.4).	17
2.4	The virial mass of a dark matter halo as a function of cosmological redshift. The mass thresholds for Pop III star formation are shown for two strengths of the LW background (high LW in gold, and low LW in red).	19
2.5	The virial mass of dark matter halos that form Pop III stars plotted as a function of redshift. The colored circles represent dark matter halos for different IMFs. The upper plot shows the virial mass of dark matter halos in the presence of a weak LW background (solid red line), while the lower plot shows the virial mass of a dark matter halo in the presence of a strong LW background (solid yellow line). In both plots, dark matter halos in the dark grey region will not form any Pop III stars due to lack of H_2 and insufficient mass that is required for the collapse of the halo. In the lower plot, less dark matter halos can form Pop III stars due the presence of a strong LW background.	20
3.1	The number of Pop III stars at a given mass as a function of mass, starting at the accepted minimum mass required for forming a Pop III star at $10M_{\odot}$	23

4.1	Heat maps of the number of PISN per halo as a function of redshift. The subplots represent the nine potential IMF slopes we consider in the model, at which the number of PISN per halo is predicted, ranging from a flat slope of $\alpha = 0.2$ to Salpeter IMF $\alpha = 2.35$	29
4.2	Apparent AB magnitude (the rest frame UV) is plotted as a function of the number of halos that form Pop III stars per arcsec ² . The triangles represent a high external LW while the circles represent a low LW background. The colors of the symbols correspond to the different IMF slopes we chose in our model. The white region shows magnitudes for Pop III stars that can only be detected by caustic crossing events. The dark grey area shows the AB magnitude at which Pop III stars can be detected by a NIRCcam pointing. The light grey area shows magnitudes where Pop III stars are potentially detectable with gravitational lensing (typical of the Frontier Fields).	31
4.3	The PISN rate curves for each of our possible slopes of the IMF. The number of PISN per year detected by a single NIRCcam pointing of JWST is plotted as a function of redshift.	32
4.4	Heat maps of the number of PISN per halo as a function of redshift for the case with a strong external Lyman-Werner Background. The maps represent the case of a maximum mass of a Pop III star of $8000 M_{\odot}$, and are plotted over a large range of possible IMF slopes.	33
4.5	The PISN rate curves for each of our possible slopes of the IMF. The number of PISN per year for a single NIRCcam pointing of JWST is plotted as a function of redshift. The redshift range goes from $z=6$ to $z=30$. The curves are plotted for the case of a strong external Lyman-Werner with a maximum mass of a Pop III star at $8000 M_{\odot}$	34
4.6	The median number of Pop III stars formed for each fate of the star as a function of the slope of the IMF.	35
4.7	The rate of PISN per year for a single NIRCcam pointing as a function of redshift.	36
4.8	The rate of PISN per year for a single NIRCcam pointing as a function of redshift. All the curves shown here are plotted for a high external LW background, with a maximum mass of $8000 M_{\odot}$	37
4.9	Heat maps of the number of PISN per halo as a function of redshift for four possible maximum masses of a forming Pop III stars. All maps represent a low external Lyman-Werner and are plotted for 9 different IMF slopes.	38
4.10	The number of PISN per year for a single NIRCcam pointing of JWST is plotted as a function of redshift for four different maximum masses of a Pop III star. The redshift range goes from $z=6$ to $z=30$ and the curves are plotted for the case with a low external Lyman-Werner.	40
4.11	The number of Pop III stars formed for each fate of the star as a function of the slope of the IMF.	41

4.12	The rate of PISN per year for a single NIRCam pointing as a function of redshift. All the curves shown here are plotted for a low external LW background, with four possible maximum masses (300, 500, 1000, and 8000 M_{\odot}).	43
5.1	The number of Pop III stars that will explode as a PISN as a function of the IMF. The purple curves are plotted for a strong Lyman-Werner background, and the green curves reflect the number of PISN in a low LW background	45
A.1	Heat map of the number of PISN per each halo at a given redshift, for an IMF with slope $\alpha = 1.0$ and an $M_{max} = 1000M_{\odot}$. Each hexagon represents the number of halos with a given number of PISN at a given redshift. The darker the shade, the greater the quantity, and vice-versa.	51
A.2	Total number of PISN in all halos at each redshift for an IMF with a slope $\alpha = 1.0$	52
A.3	The number of PISN per redshift for an IMF with slope $\alpha = 1.0$ and $M_{max} = 1000M_{\odot}$, after taking Δz into account. Note that we used $\Delta z = 0.5$ in our calculations.	53
A.4	Total number of boxes needed to make up a single NIRCam pointing as a function of redshift.	54
A.5	The number of PISN per a single NIRCam pointing as a function of redshift.	55
A.6	Rate of PISN per year as a function of redshift.	55
A.7	Total number of PISN per year per redshift, for a single NIRCam pointing. The IMF used has a slope of $\alpha = 1.0$ and $M_{max} = 1000M_{\odot}$	56

List of Abbreviations

Pop III	Population III stars
Pop II	Population II stars
Pop I	Population I stars
CMB	Cosmic Microwave Background
CDM	Cold Dark Matter
JWST	James Webb Space Telescopes
RST	Roman Space Telescope
PISN	Pair Instability Supernova
CCSN	Core Collapse Supernova
DCBH	Direct Collapse Blackhole
ISM	Interstellar Medium
IGM	Intergalactic Medium
AHF	Amiga Halo Finder
SAM	Semi Analytic Model
SED	Spectral Energy Distribution
IMF	Initial Mass Function
RAM	Random Access Memory
CPU	Central Processing Unit

Chapter 1

Introduction

The first stars in the universe, the metal free Population (Pop) III stars, play an essential role in cosmic evolution; their supernovae explosions enrich the interstellar medium (ISM) and the inter galactic medium (IGM) (Jaacks et al. 2018). This sets the stage for the enriched galaxies that follow them. Therefore, learning about the formation of this first light teaches us how subsequent, larger, and more complex structures formed.

1.1 The formation of structure

Initially, the universe was completely homogeneous and isotropic. During inflation, quantum fluctuations were suddenly expanded to, and frozen out on macroscopic scales. Over time, these small (10^{-5}) fluctuations grew until they became gravitationally unstable, and collapsed into the first dark matter halos. The dark matter halos then merged into more massive halos via hierarchical merging. Throughout this process, baryonic matter followed the dark matter into the potential wells of the dark matter halos. The first Pop

III stars form when a halo has enough coolant (H_2) for gas to cool, and sufficient gas mass to become Jeans unstable and collapse. This threshold is given by:

$$M_{vir}^{III} = \max \begin{cases} M_{H_2} = 1.905 \times 10^5 M_\odot \left(\frac{1+z}{31}\right)^{-1.5} \\ M_J = 1.36 \times 10^5 M_\odot \left(\frac{1+z}{31}\right)^{-2.071}, \end{cases} \quad (1.1)$$

where M_{H_2} is the minimum dark matter halo mass for a given redshift, z for which there is enough H_2 to cool the primordial gas, M_J is the minimum dark matter halo mass for a given redshift, where the gas has enough mass to become Jeans unstable and collapse. Both conditions must be met for Pop III stars to form in a halo. Once the first stars form, they produce, among other types of radiation, a non-ionizing background, which dissociates the H_2 that the pristine gas needs to cool. In the presence of this Lyman Werner (LW) background, a dark matter halo can only form stars if $M_{vir} > M_{LW}$ where

$$M_{LW} = 6.44 \times 10^6 M_\odot J_{21}^{0.457} \left(\frac{1+z}{31}\right)^{-3.557}, \quad (1.2)$$

and J_{21} is the strength of the LW background at a given redshift, z . However, if a halo is massive enough to shield its H_2 from the LW background, it can form Pop III stars regardless of the strength of the non-ionizing background. If a halo has a mass $M_{vir} > M_{HI}$, it will always form stars:

$$M_{HI} = 7.75 \times 10^6 M_\odot \left(\frac{1+z}{31}\right)^{1.5}, \quad (1.3)$$

where M_{HI} is the minimum dark matter halo mass to cool via HI and self shield H_2 at a given redshift, z . These thresholds are summarized in Figure 1.1.

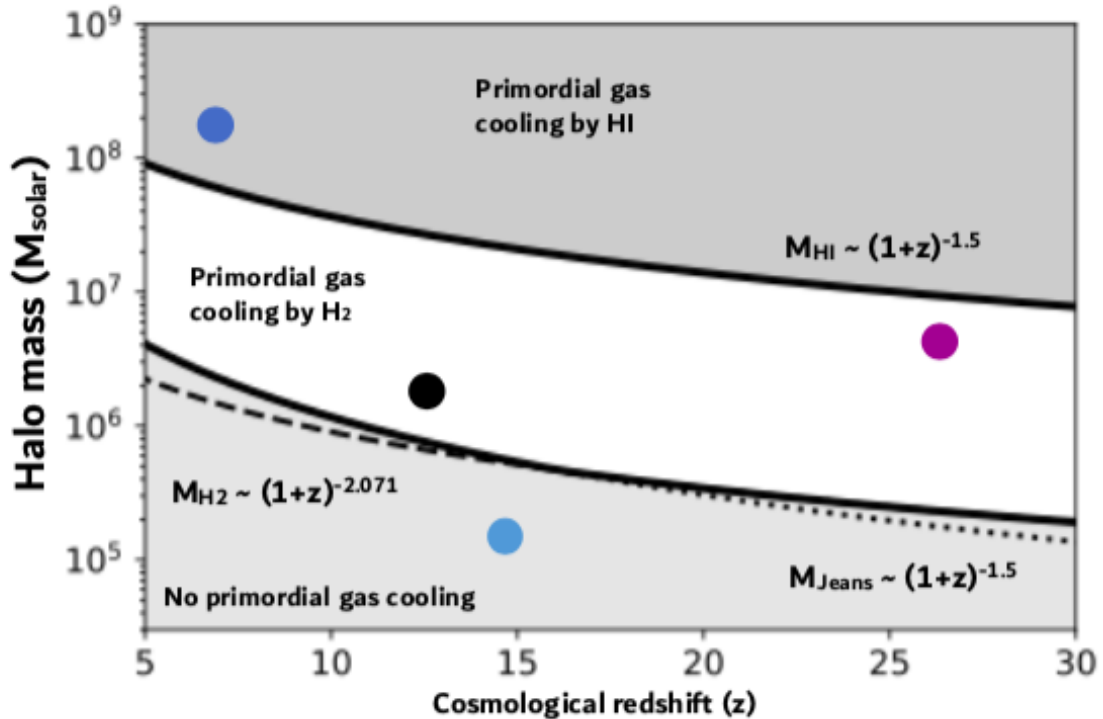


Figure 1.1: The mass of a dark matter halo as a function of cosmological redshift. (M. S. Bovill, private communication)

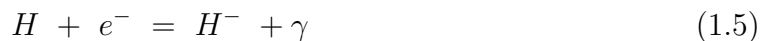
1.2 The first stars

Pop III stars form in low mass halos ($M \sim 10^5$ solar masses (M_\odot)) at cosmological redshifts $z > 20$, ending the Cosmic Dark Ages sometime during the first billion years of cosmic time (Jaacks et al. 2018a). However, they are beyond the reach of current telescopes (Gardner et al. 2006). Beyond our current knowledge that they existed and are likely more massive than later generations of metal enriched stars, very little is understood about the first stars. The reason Pop III stars are thought to be massive originates from the primary coolant available for primordial gas. The only elements that

were available to form Pop III stars were primordial hydrogen and helium created during the Big Bang. All elements heavier than helium form in the core of stars and are known as "metals". The fundamental mechanism for their formation is analogous to metal enriched stars at later epochs. When the total gas within a halo becomes larger than the Jeans mass (M_J), the gas becomes gravitationally unstable and collapses to form stars (Abel et al. 2002). The Jeans mass is described as follows:

$$M_J \sim c_s^3 G^{(-3/2)} \rho^{-(1/2)}, \quad (1.4)$$

where c_s is the adiabatic sound speed, G is the gravitational constant and ρ is the gas density. Since c_s increases with the temperature, the more rapidly the gas is able to cool, the lower the Jeans mass will become. In the modern universe, metal enriched gas primarily cools via the rotational and vibrational transitions of the CO molecule. Although there are other coolants in the modern universe (e.g. molecular hydrogen and dust), they are inefficient compared with CO . However, during the formation of the *first, metal free*, Pop III stars, neither carbon nor oxygen has formed, and the only coolant available was molecular hydrogen, H_2 . Gas present during this era had to be cooled via H_2 , which is a poor coolant in comparison to the CO available for enriched Pop II and Pop I star formation (Figure 1.2). Moreover, H_2 cannot be collisionally induced to emit photons at low temperatures. H_2 forms via two pathways, the H^- pathway:





or the H_2^+ pathway:



The abundances of H_2 asymptote to $f_{H_2} = 4.7 \times 10^{-4} (T_{vir}/1000K)^{1.54}$, where T_{vir} is the virial temperature of the dark matter halo. The relatively inefficient rotational transition of H_2 results in higher Jeans masses (Figure 1.2). Therefore, Pop III stars are thought to have been more massive than their enriched counterparts (Heger & Woosley 2002) with corresponding lifetimes of the order, or less than of a few Myr. In addition, Pop III stars are expected to have high surface temperatures due to their high masses and low metallicity, with spectral energy distributions (SEDs) peaking in the UV.

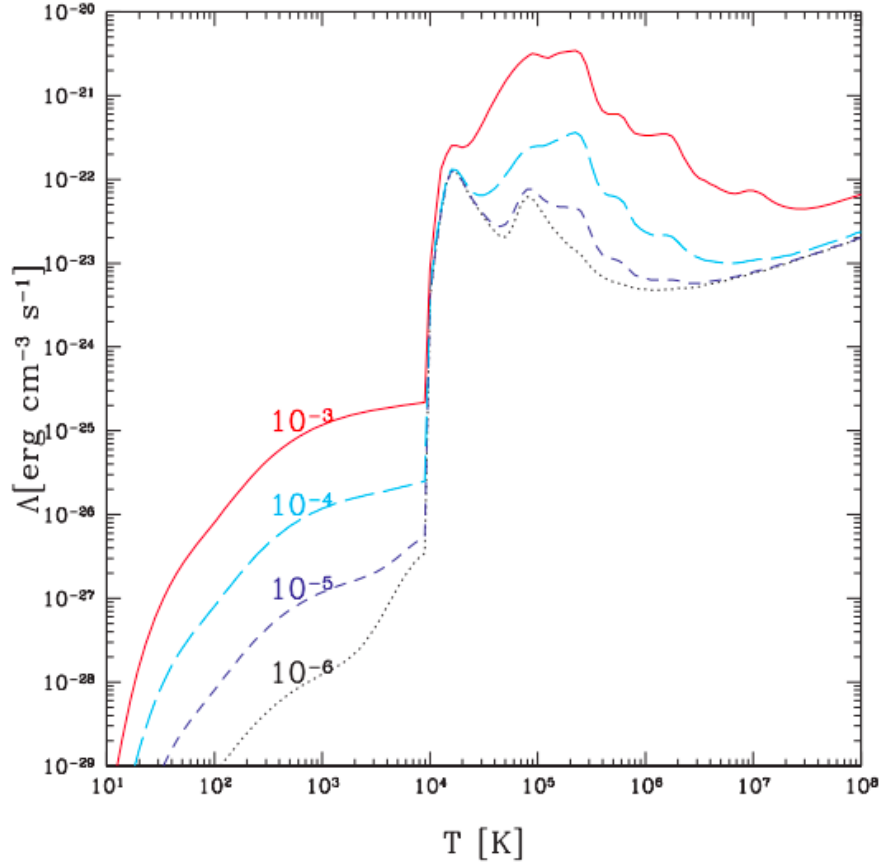


Figure 1.2: The cooling function for stars with different metallicities. Specifically, the cooling efficiency versus temperature. Low gas temperatures below $T = 10^4 K$ cannot photoionize H_2 . As a result cooling efficiency remains low below this limit. However, H_2 being dominant gas, cooling becomes more efficient beyond $10^4 K$ (Maio et al. 2007).

1.3 Fates of Pop III Stars

1.3.1 Core Collapse Supernova

For Pop III stars with masses between $8-140 M_{\odot}$, we assume they die in core collapse supernova (CCSN). The cores of these stars are composed of Fe nuclei, positrons, and electrons. Electron pressure marginally manages to balance gravity at this stage. However, when these electron-positron pairs combine to form neutrons gravity exceeds electron

pressure causing them to collapse and explode in a supernova (Mezzacappa & Messer 1999). In these supernovae explosions, the core of the massive star gravitationally collapses leaving behind a stellar mass blackhole as a remnant. As they explode, they inject their outer layers into their surrounding with energies $\sim 10^{51} \text{erg}$. The metal yield from a CCSN explosion is approximately 20% of the initial mass of the stars.

1.3.2 Pair Instability Supernova

More massive Pop III stars ($140 - 260M_{\odot}$) die in a pair instability supernova (PISN). In these supernovae, the stars blow themselves apart in extremely energetic explosions, where the brightest PISN has energy outputs of 10^{53} erg. PISN explosions leave behind no remnants and are responsible for most of the first metal enrichment processes, as their metal yield is 70% of the initial mass of the star. Collapse of these massive stars is triggered by extremely hot core temperatures which leads to production of electron and positron pairs. As they collapse, highly explosive oxygen within the star begins to ignite resulting in a massive explosion (Kasen et al. 2011).

1.3.3 Direct Collapse Blackhole

Pop III stars with masses $> 260M_{\odot}$ die in a direct collapse blackholes (DCBH), and the upper limit on their mass is unknown. It is possible that under specific conditions pristine gas of halos collapses directly into blackholes. Either process produces black holes more massive than a core collapse supernova (Agarwal et al. 2014). There is currently no

theoretical consensus for what the maximum mass of a DCBH might be, and no current observational data is available to constrain it. Figure 1.3 shows the fates for the first stars, determined by Heger & Woosley (2002) for non-rotating metal free stars (zero metallicity).

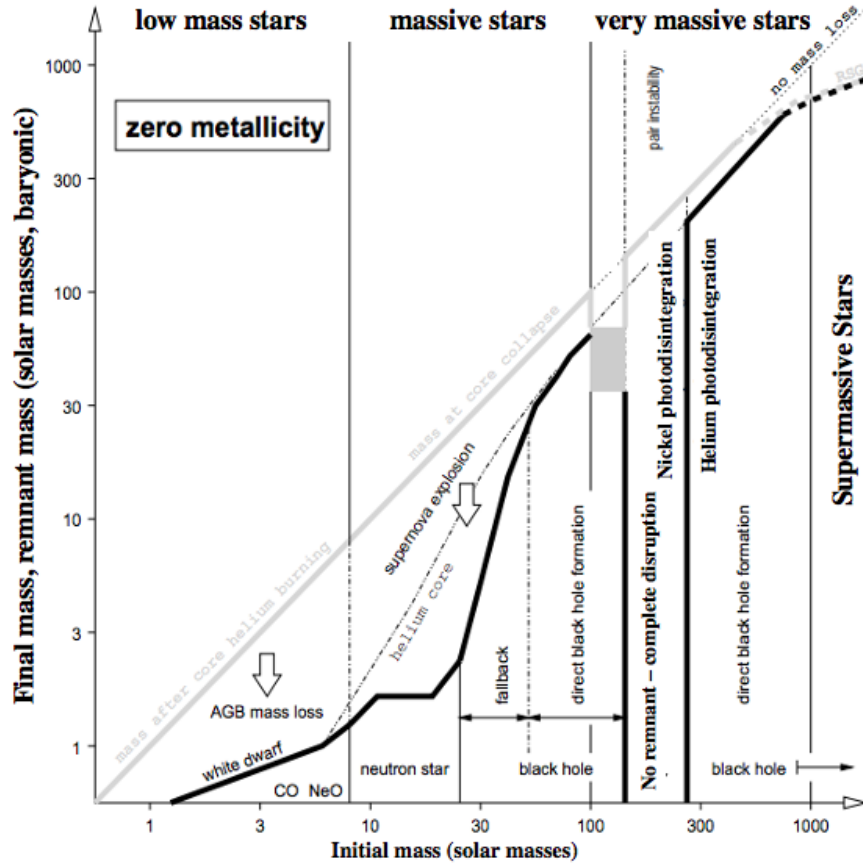


Figure 1.3: Final mass vs initial mass function of non-rotating primordial, Pop III stars ($Z = 0$) from Heger & Woosley (2002) with modifications. Collapsed remnant and mass of the star prior to the remnant when the event begins shown in thick black curve and thick gray curve respectively. Four regimes of initial mass are shown in the figure, low mass stars below $\sim 10 M_{\odot}$ that become white dwarfs; very massive stars between $\sim 100 M_{\odot}$ and $\sim 1000 M_{\odot}$; and supermassive stars above $1000 M_{\odot}$. The fates of the first stars are also shown in the figure. Pop III stars between $\sim 8 - 140 M_{\odot}$ die in CCSN, while stars with masses between $\sim 140 - 260 M_{\odot}$ die as PISN. Stars that are more massive than $\sim 260 M_{\odot}$ collapse directly into black holes.

1.4 Detection of the first stars

As direct, unmagnified, observations of Pop III stars are beyond the reach of current and future telescopes; (Jaacks et al. 2018a, Windhorst et al. 2018), we must rely on indirect methods for observational data. Pop III stars are in reach of the Near Infrared Camera (NIRCam) on JWST with gravitational lensing (Windhorst et al. 2018). However, potential rare caustic crossing events or highly magnified detections in the Frontier Fields will provide only limited information about the underlying population. One of the most promising avenues for detecting the first stars is via their deaths. A subset of Pop III stars, those with masses $140 - 260M_{\odot}$ explode in a Pair Instability Supernova (PISN). In PISN, the stars blow themselves apart in explosions (10^{53} erg) a hundred times more energetic than that for a core collapse supernova (Whalen et al. 2013). PISN are bright enough to be detected by future telescopes (e.g. JWST and the Roman Space Telescope; Whalen et al. 2013, Fox et al. 2021). However, extracting the astrophysics of Pop III stars from PISN rates is complex, and requires observations to be analyzed in concert with theoretical work, which encompasses the relatively unexplored parameter space of the mass distribution of the first stars.

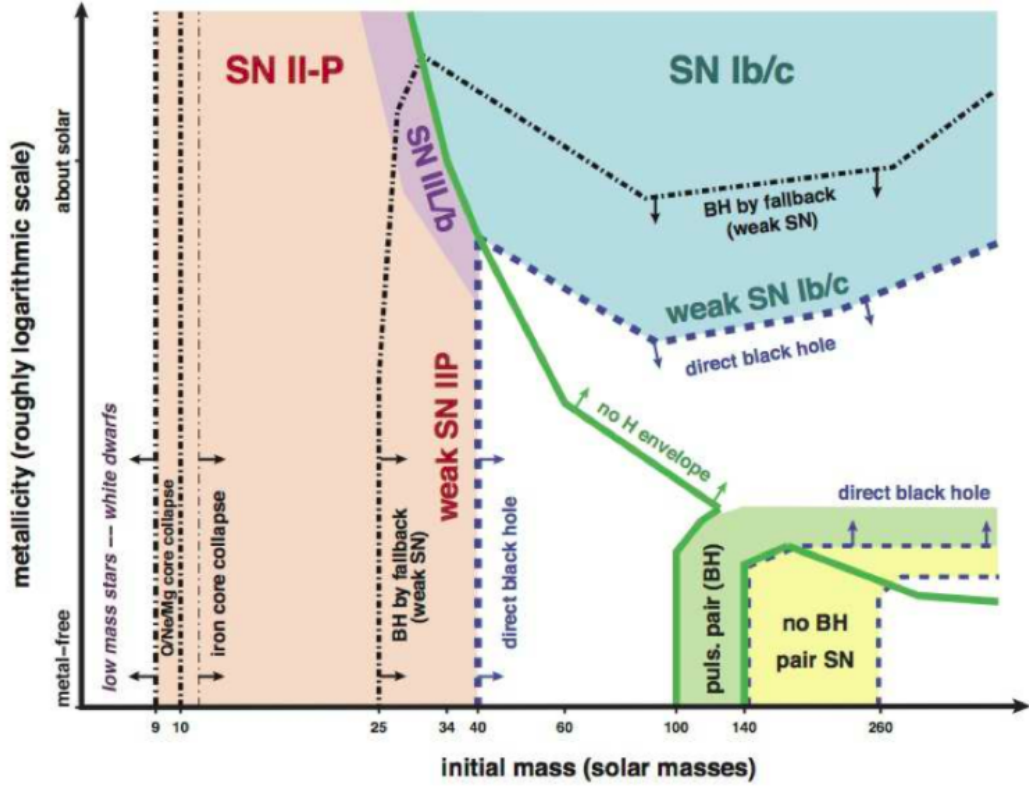


Figure 1.4: Stars metallicity as a function of their initial masses. Our area of interest is the yellow region, which corresponds to very low metallicity stars with very high masses. These stars are within the range of mass for PISN. This figure is reproduced from Heger et al. (2003).

In this work, we present predictions for the PISN rates for various mass distributions using a semi-analytic model developed in (Bovill et al. *submitted*). In Section 2, we describe the simulations used in this project, and in Section 3, we describe in detail the relevant physics of the semi-analytic model, in particular, the rate predictions for PISN. In Chapter 4, we present our predictions for the dependence of PISN rates on the mass distribution of Pop III stars including the slope of the initial mass function (IMF), the minimum and the maximum masses. The initial mass function of Pop III stars is the distribution of their masses at the time of their formation. We discuss our conclusions in Section 5.

Chapter 2

Simulations

We model Pop III stars as follows (Figure 2.1): First, we run an N-body simulation with sufficient resolution to resolve all possible sites of star formation, for the first billion years of cosmic evolution. Second, we identify the location of dark matter halos within the simulation, and link them through cosmic time into a merger tree. Third, we use the semi-analytic model to add the physics of gas cooling, as well as Pop III star formation into the simulation.

The N-body simulation that we used in this work is 2 Mpc/h comoving and evolves from $z = 150$ to $z = 6$ with $N = 512^3$ with a dark matter particle mass of $\approx 10^3 M_\odot$. A comoving length is related to the physical length by $l_{comoving} = (1 + z)l_{physical}$, so at the redshifts of interest, our box is *roughly* 200 kpc on a side. We robustly resolve halos with $M > 10^5 M_\odot$ with 100 particles per halo, allowing us to resolve all potential sites of Pop III star formation. Simulations were run with the public N-body code Gadget 2 (Springel 2005) on initial conditions generated by The Multi-Scale Initial Conditions for cosmological simulations (MUSIC, Hahn & Abel 2011) and analyzed with Amiga Halo

Finder (AHF) (Knollmann & Knebe 2009, Gill et al. 2004) and consistent trees (Behroozi et al. 2012). Though the development of these algorithms was not part of this thesis, the details of how they work is explained in more detail in Sections 2.1 and 2.2. As Pop III stars only form in metal free dark matter halos, we use the model developed in (Bovill et al. *submitted*) to determine which halos in the simulation remain pristine at a given redshift, for a large range of possible Pop III mass distributions. Further information on our PISN rate calculation is in Chapter 3.

We show our methodology in Figure 2.1. We now discuss each step in more detail in the next sections.

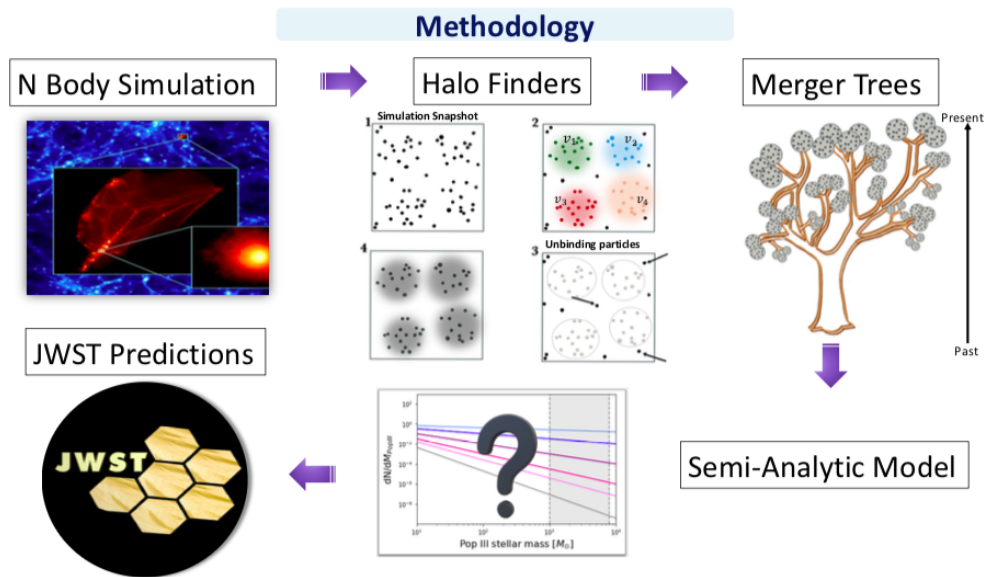


Figure 2.1: Flow chart of the steps we use to model the first stars, with the goal of making predictions for JWST.

2.1 AMIGA Halo Finders

Halo finders explore the simulation to find gravitationally bound clumps of dark matter particles. Note, the dark matter particles in our simulation are traces of the distribution of dark matter in the simulation box, and their mass is chosen based on the mass of the dark matter halos we want to resolve. Each snapshot of the N-body simulation provides the positions, velocities, and masses of the dark matter particles. The bound clumps of dark matter found by the halo finder are dark matter halos, and in addition to determining their location and mass, the halo finder determines the properties of the dark matter halos (ie. v_{max} , R_{vir} and spin). In our work, we use the halo finder (AHF) developed by (Knollmann & Knebe 2009, Gill et al. 2004). AHF is a density based halo finder. It calculates the densities of dark matter particles to identify potential groupings of particles. The density fields are used to find cosmological structures, before AHF identifies possible halos within them as density peaks above the overall cosmic density field. The halo finder continues to mark isolated refinements until all halos are identified, including substructures, down to the resolution limit ($N \simeq 20$). Once the dark matter halos are identified, AHF removes gravitationally unbound particles by identifying particle positions, and obtaining the escaped velocity v_{esc} at each position. If a particle's velocity is greater than the escape velocity at that point it is removed from the halo and the halo properties recalculated. While density based halo finder, such as AHF are extremely efficient at finding structures with low numbers of dark matter particles, the mesh grids used to calculate the densities require significant CPU time and RAM.

The mass distribution, or mass function, of dark matter halos in our simulation at three redshifts is shown in Figure 2.2. Once the halos are found, the next step is to link them through time to form merger trees.

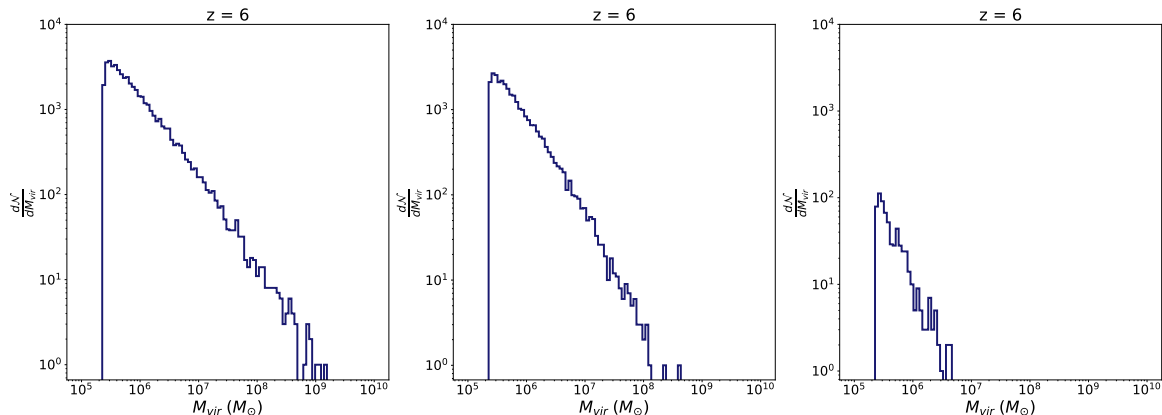


Figure 2.2: Halo mass function at different redshifts. This plot shows the number of halos per dark matter virial mass $\left(\frac{dN}{dM_{vir}}\right)$ at redshifts $z = 6, 10, 20$, respectively.

2.2 Merger Trees

A merger tree code links the dark matter halos through cosmic time and outputs the history of every halo in the simulation. The resulting merger trees tell us what halos were progenitors (parent halos of an earlier redshift) and where they were and their properties (virial mass, radius, etc.). The merger trees for the entire simulation are called forests. We use the merger tree code consistent-trees (Behroozi et al. 2012). Consistent-trees examines the future time-step of descendant halos to identify which halos have the largest fraction of particles belonging to that halo. These are identified as the most massive progenitors. It then goes back in time to identify those particles and their respective progenitor halos. Once candidate progenitor halos are found, the code calculates the

gravitational acceleration between halos, which is then evolved to calculate their respective velocities and positions. These positions and velocities are used to link progenitor halos. If a progenitor is missing for one time-step, consistent-trees places a halo in its position using the velocities and positions calculated using gravitational evolution. However, halos with missing progenitors for several time-steps are removed. If a previous halo has no descendants and is located close to other halos, consistent-trees assumes that a merger has occurred by applying a strong tidal force across that halo. The process is repeated until the end of the simulation.

We next add baryons into the dark matter only N-body simulation by way of a semi-analytic model.

2.3 Semi Analytic Model

In this section we describe the physics included in the SAM.

2.3.1 Lyman-Werner Background

While their lifetimes are short, the first stars do shine. The non-ionizing ultraviolet background, Lyman Warner, produced by these stars dissociates H_2 suppressing the formation on Pop III stars in low mass halos. The number density of LW photons n_{LW} produced by the massive ($M > 8M_\odot$) Pop III stars is given by:

$$J_{21} = 1.6 \times 10^{-65} \left(\frac{n_{LW}}{1Mpc^{-3}} \right) \left(\frac{1+z}{31} \right)^3 \text{ ergs}^{-1} \text{ cm}^{-2} \quad (2.1)$$

where J_{21} is the strength of the LW (Stiavelli 2009) Therefore,

$$n_{LW} = 8 \times 10^{60} M_{III} + 8 \times 10^{59} M_{II}(m_{II} > 8M_{\odot}) \quad (2.2)$$

where M_{III} and M_{II} are the total mass of Pop III and II stars, respectively, and m_{II} is the individual mass of a Pop II star.

We also need to consider the LW due to the formation of stars inside the box, namely Pop II stars of masses $M > 8 M_{\odot}$. However, if the box size is much smaller than the physical scale of the LW, we must add an additional component of LW radiation coming from stars outside of our simulation box.

$$J_{21}^{TOT} = J_{21} + J_{21}^{external} \quad (2.3)$$

where J_{21}^{TOT} is the total LW. For smaller boxes, the external Lyman Warner's effect from outside the box is approximated.

The two J_{21} external backgrounds considered in this thesis from (Trenti & Stiavelli 2009) are shown in Figure 2.3.

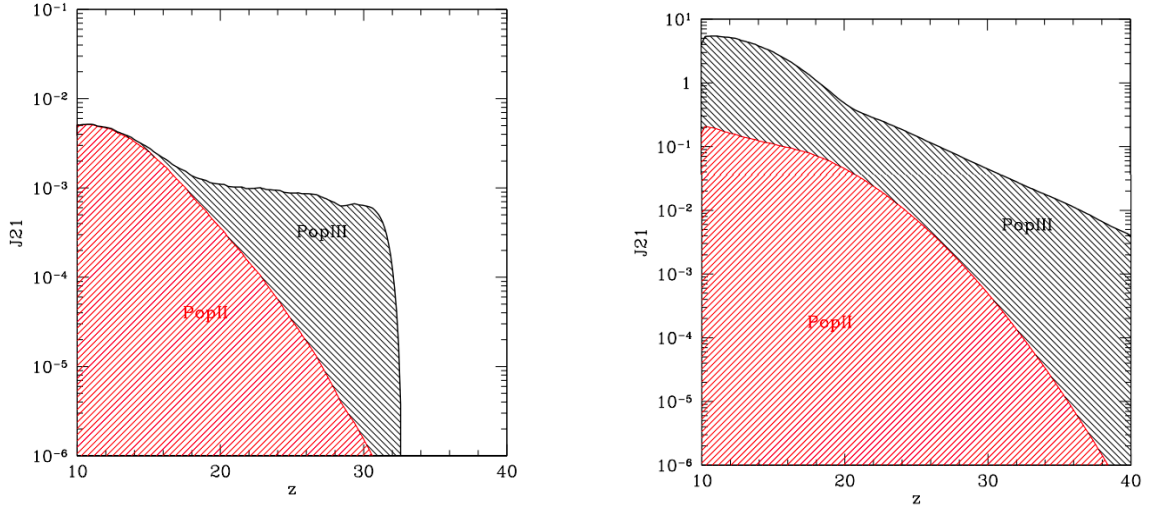


Figure 2.3: The two cases of the Lyman-Werner backgrounds used in our SAM plotted as a function of redshift. These figures are taken from Figures 2 and 7 from Trenti & Stiavelli (2009), respectively. The left figure represents the low LW background (red curve in Figure 2.4), and the right figure is for a high LW background (gold curve in Figure 2.4).

2.3.2 Metal Enrichment

The end of the Pop III era marks an essential transition point between unenriched and enriched star formation. To form a Pop III star, a halo must have a gas of extremely low metallicity ($Z < 10^{-3.5}$). To confirm a halo has this low metallicity, two main conditions must be met:

1. If any progenitor formed stars, our simulation assumes that this halo is enriched and will form Pop II stars.
2. The second requirement is that no progenitor halos were enriched by supernova ejecta from stars in nearby halos.

We need to calculate how far the metal content injected by nearby Pop III supernovae travels, to accurately decide whether or not a progenitor halo will be polluted. Our

model considers this problem by calculating the total amount of energy produced by the supernovae and injected into the ISM/IGM (E_{SN}). We assume the lifetime of a Pop III star is ~ 3 Myr. The same calculation is performed for Pop III and II (second generation of stars) halos. For a Pop III halo, E_{SN} is:

$$E_{SN} = N_{PISN} \cdot 10^{53} \text{erg} + N_{CCSN} \cdot 10^{51} \text{erg} \quad (2.4)$$

where N_{PISN} is the number of PISN in a halo, and N_{CCSN} is the number of CCSN in a halo, each multiplied by their associated energies, to get the total amount of energy produced by SN.

For any star forming halo, we then determine the halo mass required to contain the ejecta $M_{contain}$ through:

$$M_{contain} = 7.96 \times 10^6 M_{\odot} \left(\frac{E_{SN}}{10^{51} \text{erg}} \right)^{3/5} \left(\frac{1+z}{31} \right)^{-3/5} \quad (2.5)$$

We now determine the distance that the ejecta has traveled

$$\frac{E_{SN}}{f_b G} = \frac{(M_{vir} + \frac{4\pi}{3}(1 - f_{coll}(z))\rho_0(1+z)^3(R_{ejecta}^3 - R_{vir}^3))^2}{R_{ejecta}} \quad (2.6)$$

where E_{SN} is the total energy of supernova in the halo, f_b is the baryon fraction, G is the gravitational constant, M_{vir} is the virial mass of the halo, f_{coll} is the halo collapse fraction at a given redshift, z and R_{ejecta} is the maximum radius of the enriched ejecta.

We then determine which nearby halos have been enriched by the ejecta.

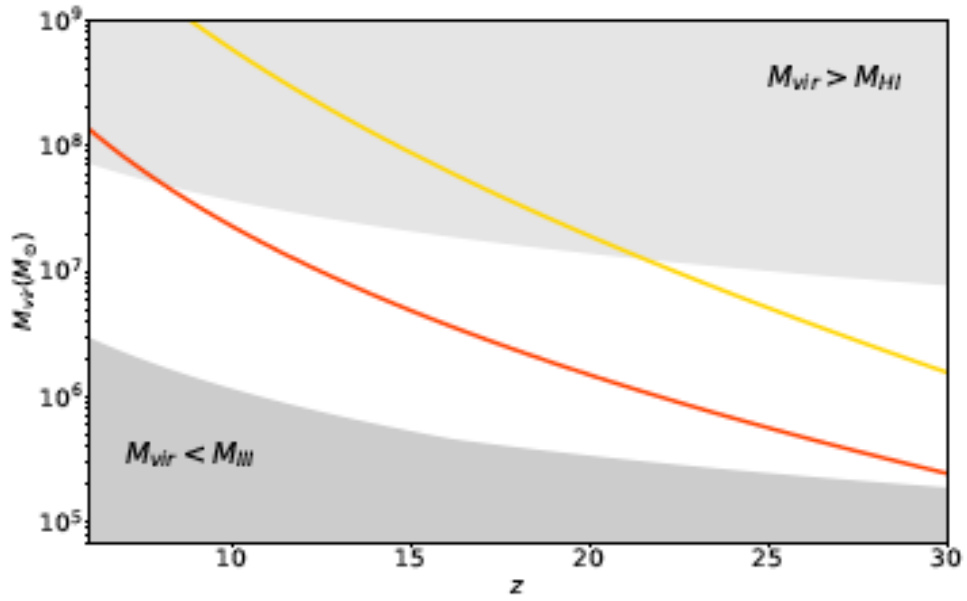


Figure 2.4: The virial mass of a dark matter halo as a function of cosmological redshift. The mass thresholds for Pop III star formation are shown for two strengths of the LW background (high LW in gold, and low LW in red). Whether a dark matter halo will be able to form Pop III stars will depend on different factors: in the dark grey region, a dark matter halo will either be unable to form stars due to insufficient amount of coolant (H_2), or mass for the required collapse. However, in the light grey region, the dark matter halos have high enough masses to protect their H_2 from dissociating by the LW background.

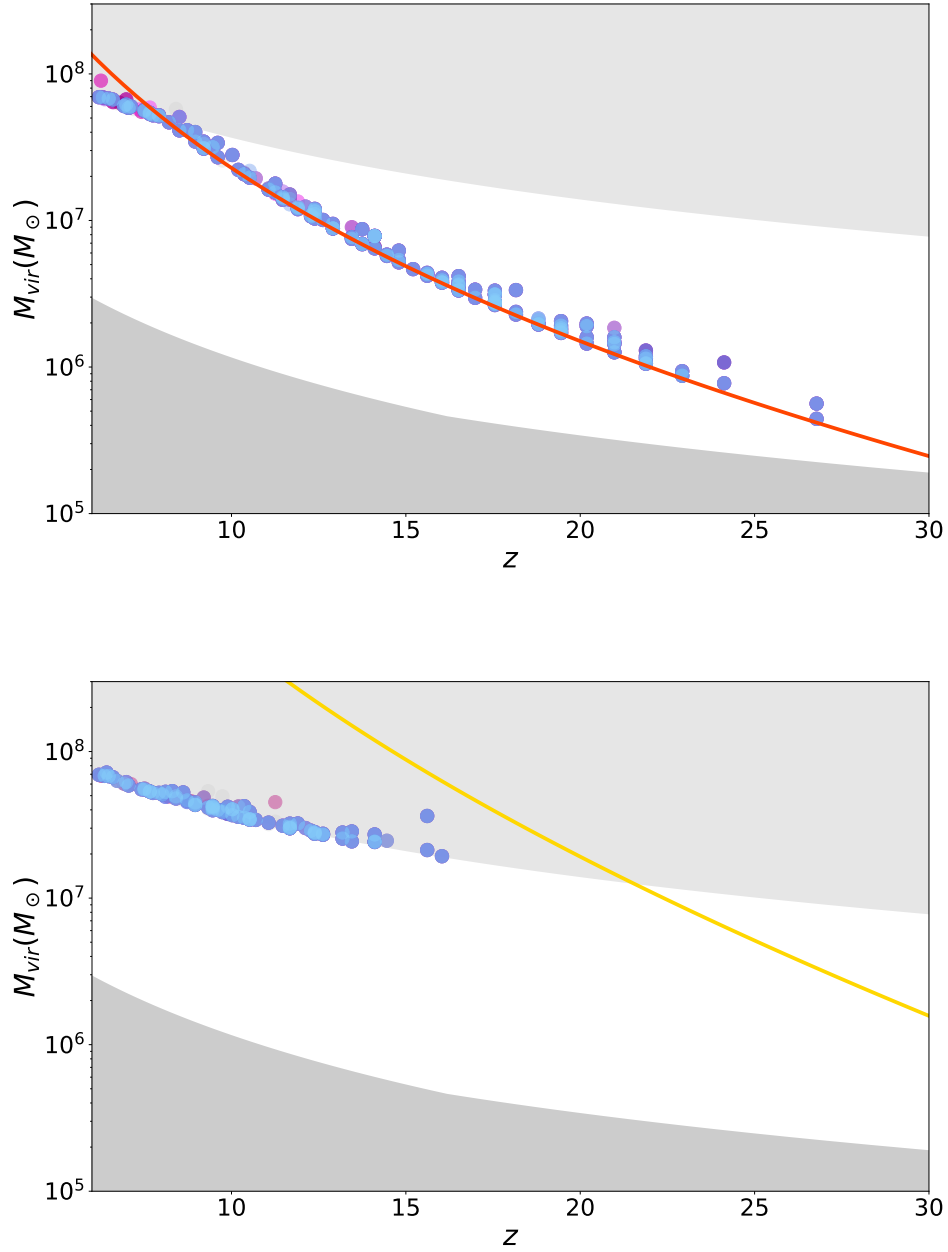


Figure 2.5: The virial mass of dark matter halos that form Pop III stars plotted as a function of redshift. The colored circles represent dark matter halos for different IMFs. The upper plot shows the virial mass of dark matter halos in the presence of a weak LW background (solid red line), while the lower plot shows the virial mass of a dark matter halo in the presence of a strong LW background (solid yellow line). In both plots, dark matter halos in the dark grey region will not form any Pop III stars due to lack of H_2 and insufficient mass that is required for the collapse of the halo. In the lower plot, less dark matter halos can form Pop III stars due the presence of a strong LW background.

Chapter 3

Modeling the Pair Instability

Supernovae Rate

In order to calculate the rate of observed PISN, we need to determine the number of stars that form in the mass range for PISN for a given IMF. Despite the uncertainty surrounding it, the IMF for Pop III stars is not always treated as a free parameter. Either using a single IMF (Wise et al. 2012, Ricotti et al. 2016, Park et al. 2021a) or exploring a limited number of potential IMFs (Jaacks et al. 2018b, Behroozi et al. 2012). In our work, we use a wide range of possible slopes for the IMF of Pop III stars and treat not only the slope of the IMF, but the minimum and maximum masses of Pop III stars as free parameters.

3.1 Pop III IMF

We assume the Pop III IMF is a power-law:

$$dN/dM = AM^{-\alpha} \quad (3.1)$$

where α is the slope of the IMF. Due to the uncertainty in the slope of the Pop III IMF, we consider a range of potential IMF power law slopes, specifically we explore $\alpha = [0.2, 0.5, 0.8, 1.0, 1.2, 1.5, 1.8, 2.1, 2.35]$ (Figure 3.1). The highest slope ($\alpha = 2.35$) is the Salpeter IMF for Pop I stars (Salpeter 1955).

The normalization of the mass function is determined by two quantities. The first quantity, the total mass available to form stars, is determined by the mass of the gas available. For Pop III stars, the maximum potential mass is given by:

$$M_{III} = \epsilon_{III}M_g = \epsilon_{III}f_bM_{vir} \quad (3.2)$$

where M_g is the mass of the gas in the halo, f_b is the cosmic baryon fraction, ϵ_{III} is the star formation efficiency of Pop III stars, and M_{vir} is the virial mass of the halo. Note that in addition to the Pop III IMF, the star formation efficiency is also a parameter in the model. For this work, we use the fiducial value from Trenti & Stiavelli (2009), $\epsilon = 0.01$.

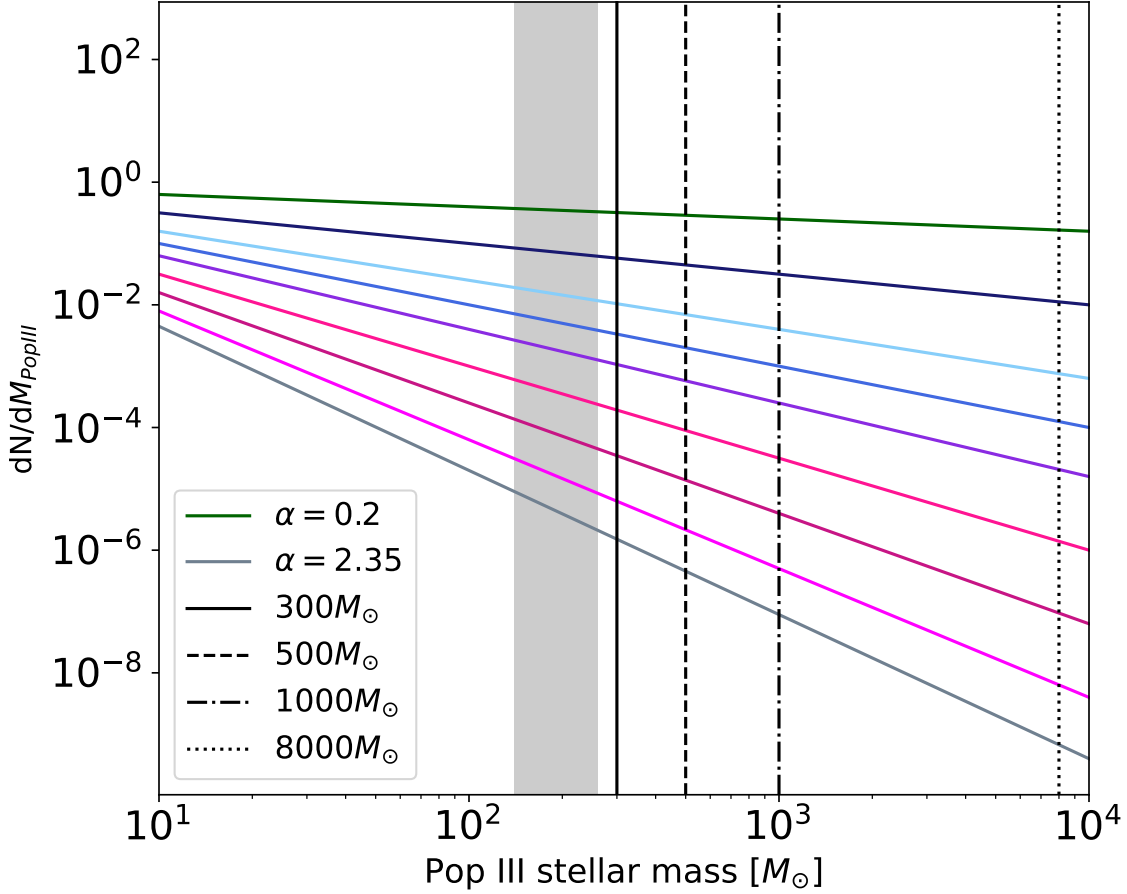


Figure 3.1: We plot the number of Pop III stars at a given mass as a function of mass, starting at the accepted minimum mass required for forming a Pop III star at $10M_{\odot}$. The curves represent nine potential slopes of the Pop III initial mass functions. The black curve ($\alpha = 2.35$) is the Salpeter IMF. The grey area represents the mass range for stars exploding in a PISN ($140 - 260M_{\odot}$; Heger & Woosley 2002).

The second quantity that can normalize the mass function is the number of stars that form. For Pop III stars this is determined by the fragmentation of primordial gas. The inefficient cooling of primordial gas limits the fragmentation of the collapsing gas in the halo. As such, for a halo with a given M_{vir} at a redshift z , the maximum number of

fragments of the primordial gas, N_{frag} is given by:

$$N_{frag} = 9.12 \left(\frac{M_{vir}}{10^6 M_\odot} \right)^{4/3} \left(\frac{1+z}{31} \right)^2 \quad (3.3)$$

where z is the redshift and M_{vir} is the virial mass of the halo. Determining how these two normalizations affect the PISN rates requires an in-depth look at how we populate the Pop III IMF.

3.1.1 How is our model populating the IMF?

The standard method in SAMs is to populate initial mass functions statistically. The initial mass function is normalized by the total mass of stars M_{tot} through the following equation:

$$M_{tot} = \int_{m_{min}}^{m_{max}} A_M m^{1-\alpha} dm \quad (3.4)$$

where m_{min} is the minimum stellar mass, m_{max} is the maximum stellar mass, and A_m is the normalization given by:

$$A_m = (2 - \alpha)(M_{tot}) \times (m_{max}^{2-\alpha} - m_{min}^{2-\alpha})^{-1} \quad (3.5)$$

Once the mass function is normalized we can then obtain the number of stars N in a given mass range, m_{min} to m_{max} :

$$N = A_M \int_{m_{min}}^{m_{max}} m^{-\alpha} dm \quad (3.6)$$

Specifically, the number of PISN is given by:

$$N_{PISN} = A_M \int_{140M_{\odot}}^{260M_{\odot}} m^{-\alpha} dm \quad (3.7)$$

In this standard method of populating the IMF, a halo of a given mass M_{vir} and redshift z with a given IMF will have the exact same mass distribution of Pop III stars, and critically, the same number of PISN. However, IMFs are actually randomly populated according to an underlying probability distribution, which is given by the IMF (see Section 3.2 for more detail). In particular, at high masses, the number of stars at a given mass is stochastic and is determined by small number statistics. This is especially important when dealing with PISN. The high energies and metal yields of PISN make them engines of metal enrichment. Therefore, for Pop III stars, randomly populating the IMF captures the initial physics of the enrichment of the IGM, and the eventual end of the Pop III era. In addition to capturing the stochasticity of populating the IMF in the PISN mass range, for primordial gas, we must account for both the maximum mass in stars and the inefficient fragmentation of primordial gas. Since we know that stars in the mass range of 140-260 M_{\odot} explode in a PISN, we can determine the number of PISN in a typical halo at a given redshift for normalization by mass:

$$N_{PISN}^M = A_M \int_{140M_{\odot}}^{260M_{\odot}} m^{-\alpha} dm \quad (3.8)$$

and by number of fragments:

$$N_{PISN}^N = A_N \int_{140M_{\odot}}^{260M_{\odot}} m^{-\alpha} dm \quad (3.9)$$

where A_M is the normalization by mass from above and A_N is the normalization by number of fragments given by:

$$A_N = (1 - \alpha)(N_{frag}) \times (m_{max}^{1-\alpha} - m_{min}^{1-\alpha})^{-1} \quad (3.10)$$

where m_{min} and m_{max} are the minimum and maximum masses for Pop III stars (m_{max} values considered in this work are shown in Figure 3.1).

3.2 Random population of the IMF

Without observational data on PISN rates, we have no way of determining whether we should normalize the mass function by the number of fragments or the total potential mass in Pop III stars. Therefore, we use a novel approach to populate the Pop III IMF. First, we randomly populate an IMF with a given α , m_{max} , m_{min} with 10^6 stars. We then only keep the stars up to the total mass available for Pop III star formation given by Equation 3.2. If the number of remaining stars $N_{III} > 6 * N_{frag}$, we truncate the number of stars so that $N_{III} = 6 * N_{frag}$. The factor of 6 is based on the number of Pop III stars that form in a given fragment in hydrodynamical simulations (Susa et al. 2014). While the probability of a star being in the mass range for the PISN is drawn from the IMF, the actual number of PISN is determined by this random population of

the IMF, and subsequent truncation. Therefore two halos of the same mass, at the same redshift, may have different numbers of PISN. If the IMF is randomly populated a high number of times, N_{PISN} should converge on one of the two analytical estimates. Whether it converges to the normalization by mass or number or somewhere in between requires further study.

Chapter 4

Results

Here we present our results for the dependence of the number and rate of PISN on the Pop III IMF, as well as on the maximum mass of a Pop III stars. Exploration of the the dependence on the minimum mass is a subject of future study. Since the size of our box is well below the physical scale of the non-ionizing UV (LW) background, we use two possible external LW backgrounds. We use two of the LW backgrounds calculated in (Trenti & Stiavelli 2009), one high and one low (shown in Figure 2.4). As the high LW background suppresses all Pop III star formation in low mass halos for $z > 15$, we focus our initial analysis on the low LW case. The maximum mass of a Pop III star is unknown. However, some studies (Wagoner 1969, Abel et al. 2002) suggest that stable, super-massive, stars with masses above ($10^4 M_\odot$) could exist. As such, we select an estimate $m_{max} \approx 8000 M_\odot$ and focus our initial analysis on the dependence of the number and rates of the PISN on the IMF slope. Throughout the work presented here, we assume a minimum Pop III mass of $10 M_\odot$. Figure 4.1 shows a heat map for the number of PISN forming in each halo for each of our IMFs as a function of redshift.

Note that the darkest hexagons in the heat maps indicate the highest number of halos in which a certain number of PISN is present at a certain redshift. As mentioned in Section 3, the slopes of the IMF range from a flat IMF ($\alpha = 0.2$) to a bottom-heavy Salpeter IMF ($\alpha = 2.35$) (Figure 3.1).

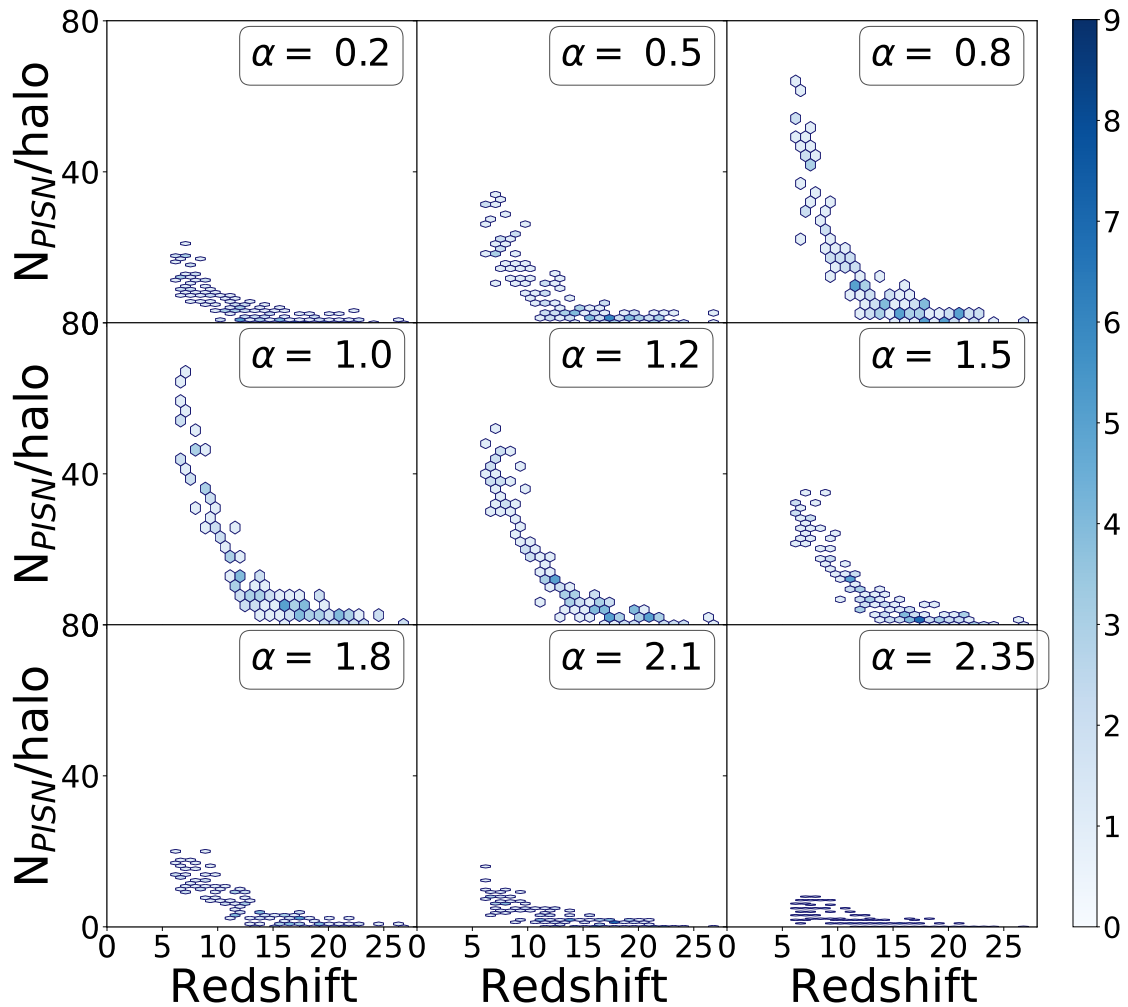


Figure 4.1: Heat maps of the number of PISN per halo as a function of redshift. The subplots represent the nine potential IMF slopes we consider in the model, at which the number of PISN per halo is predicted, ranging from a flat slope of $\alpha = 0.2$ to Salpeter IMF $\alpha = 2.35$.

As the slope of the IMF decreases, the probability a high mass star in the PISN mass range forms increases. This leads to a prediction that the number of PISN per halo should increase with a decreasing slope of the IMF. However, as seen in Figure 4.1, this is not the case. For steeper, more bottom-heavy IMFs, the prediction holds. However, at an IMF slope of $\alpha = 1.0$, the number of PISN peaks, then starts decreasing as the IMF slope continues to decrease, becoming more and more top-heavy. Before exploring the reason for this turnaround in the number of PISN in a given halo, we look at how strong of an effect it has on the predictions for the observed rates of PISN.

4.1 PISN Rate Calculations

Here, we briefly summarize the procedure for converting the number of PISN forming in each halo (Figure 4.1) into predictions for the observed rates of PISN. A more detailed and comprehensive description of this conversion is in Appendix A. Our final goal is to determine the rate of PISN per year observed in a single NIRCcam pointing. To do this, we need to determine the total number of PISN at each redshift in the simulation before smoothing this over a given Δz to account for the width of the NIRCcam filters. Note, that the chosen filters in Figure 4.2 correspond to the redshift range of interest ($6 > z > 20$) for the source emitting in the rest frame UV. We then determine the number of NIRCcam pointings required to observe our simulation box at a given redshift. The numbers of PISN are converted to rate by first accounting for the 10 Myr between outputs in the simulation, and then including the effects of time dilation due to the expansion of spacetime. The latter is done by multiplying our rate by $(1 + z)$

(Weinmann & Lilly 2005). Figure 4.3 shows the PISN rate curves for a single NIRCcam pointing for the full range of our chosen IMF slopes. N_{PISN} seems low (1 or less per year) in this plot, which implies that the detection of PISN will require a larger number of NIRCcam pointings, observed over a length of time longer than the nominal length of the primary JWST missions (10 years). This suggests that while JWST *might* detect PISN, the Roman Space Telescope with its larger field of view (~ 100 larger than NIRCcam's) is the ideal instrument for such studies (Fox et al. 2021).

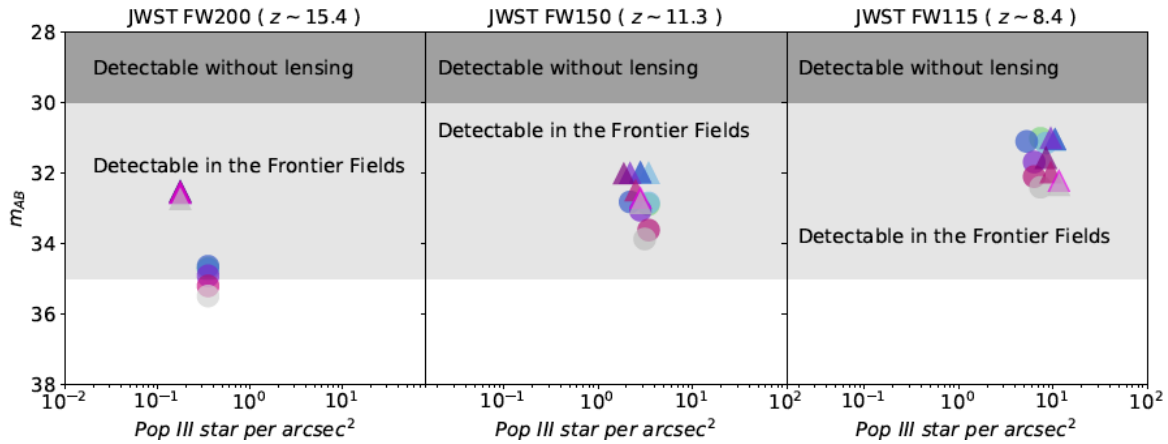


Figure 4.2: Apparent AB magnitude (the rest frame UV) is plotted as a function of the number of halos that form Pop III stars per arcsec². The triangles represent a high external LW while the circles represent a low LW background. The colors of the symbols correspond to the different IMF slopes we chose in our model. The white region shows magnitudes for Pop III stars that can only be detected by caustic crossing events. The dark grey area shows the AB magnitude at which Pop III stars can be detected by a NIRCcam pointing. The light grey area shows magnitudes where Pop III stars are potentially detectable with gravitational lensing (typical of the Frontier Fields).

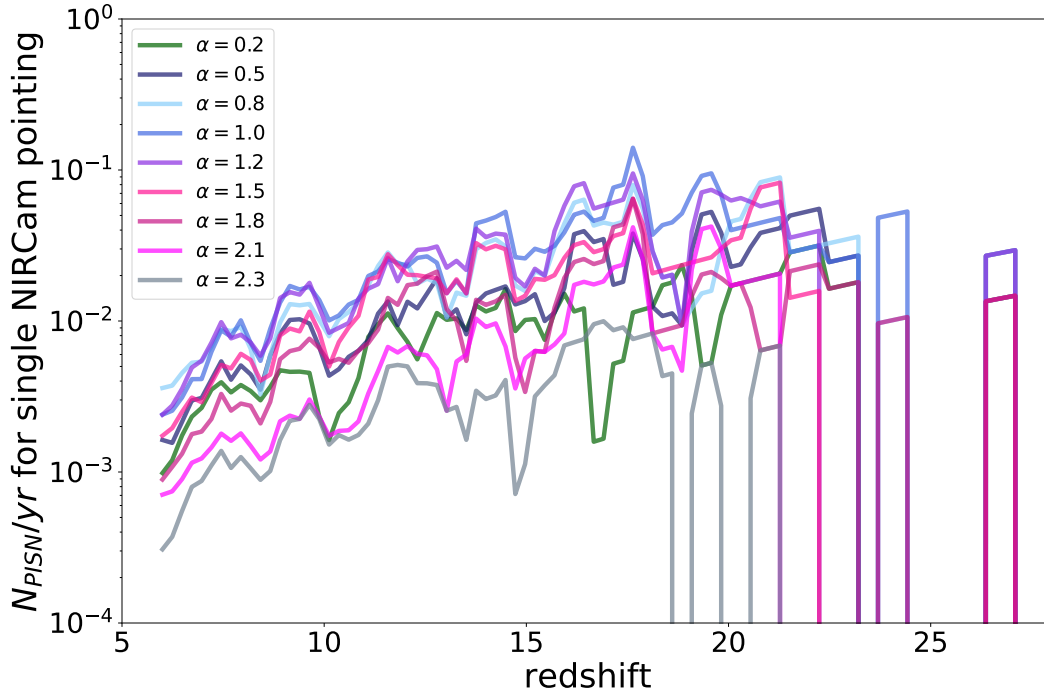


Figure 4.3: The PISN rate curves for each of our possible slopes of the IMF. The number of PISN per year detected by a single NIRCcam pointing of JWST is plotted as a function of redshift. The redshift range goes from $z=6$ to $z=30$. The curves are plotted for the case of a weak Lyman-Werner with a maximum mass of a Pop III star in the model at $8000 M_{\odot}$. The grey curve is for an enriched IMF ($\alpha = 2.35$)

We find that the unexpected turnaround in the number of PISN per halo at $\alpha = 1.0$ carries through to the predictions for the observed rates. For $\alpha < 1.0$, the number of PISN observed in a year by one NIRCcam pointing eventually drops to half of its peak value for our most top heavy IMF ($\alpha = 0.2$)

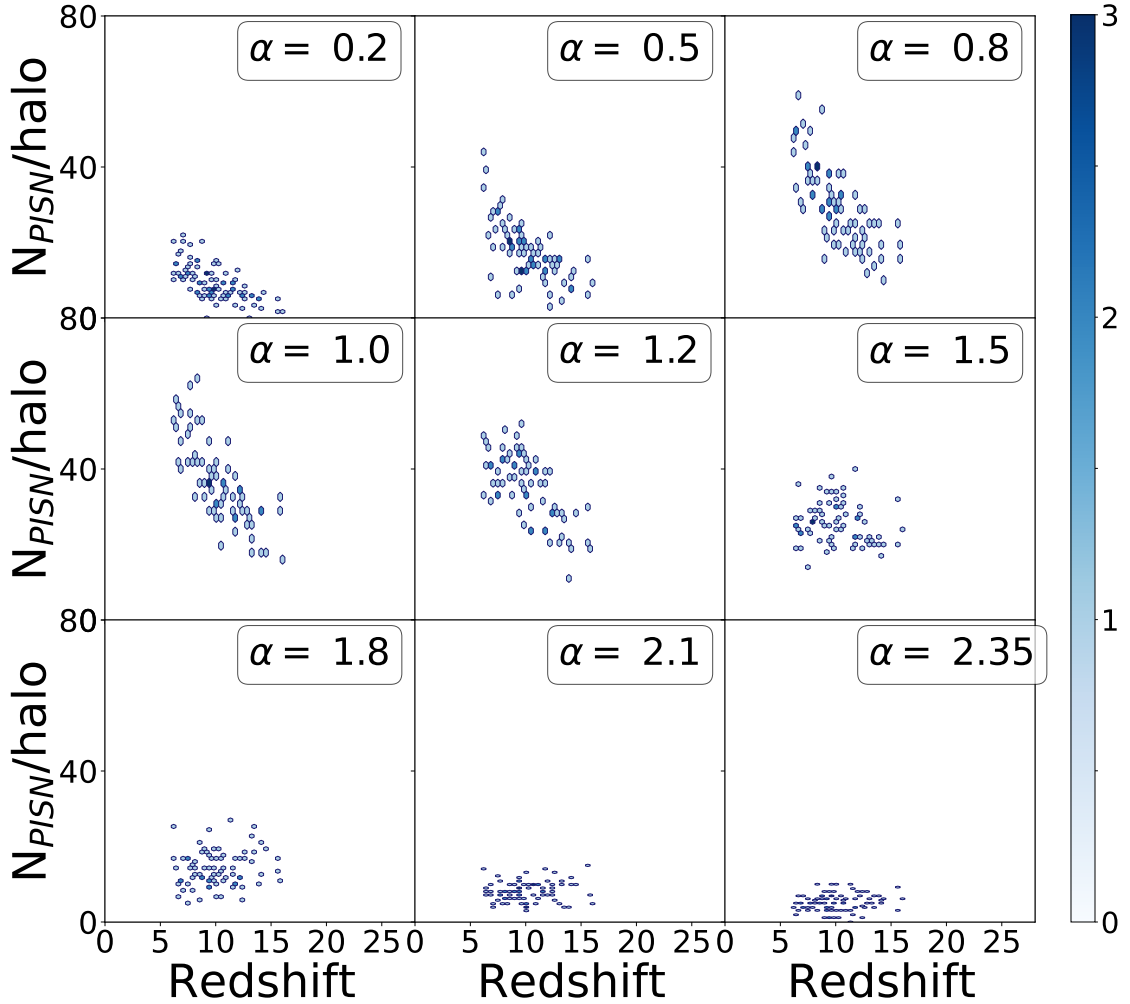


Figure 4.4: Heat maps of the number of PISN per halo as a function of redshift for the case with a strong external Lyman-Werner Background. The maps represent the case of a maximum mass of a Pop III star of $8000 M_{\odot}$, and are plotted over a large range of possible IMF slopes.

We next confirm that our results are independent of our choice of the external LW background. Figure 4.4 shows a heat map of the number of PISN forming in each halo, in the presence of a strong LW. As expected, in Figure 4.4, no Pop III stars, and therefore, no PISN form in halos at $z > 15$, which is at later times than for low LW case ($z = 25$).

For the high external LW case we also notice a similar turn around at an IMF slope of $\alpha = 1.0$. Therefore, the existence and location of the turnaround is independent of the strength of the LW background.

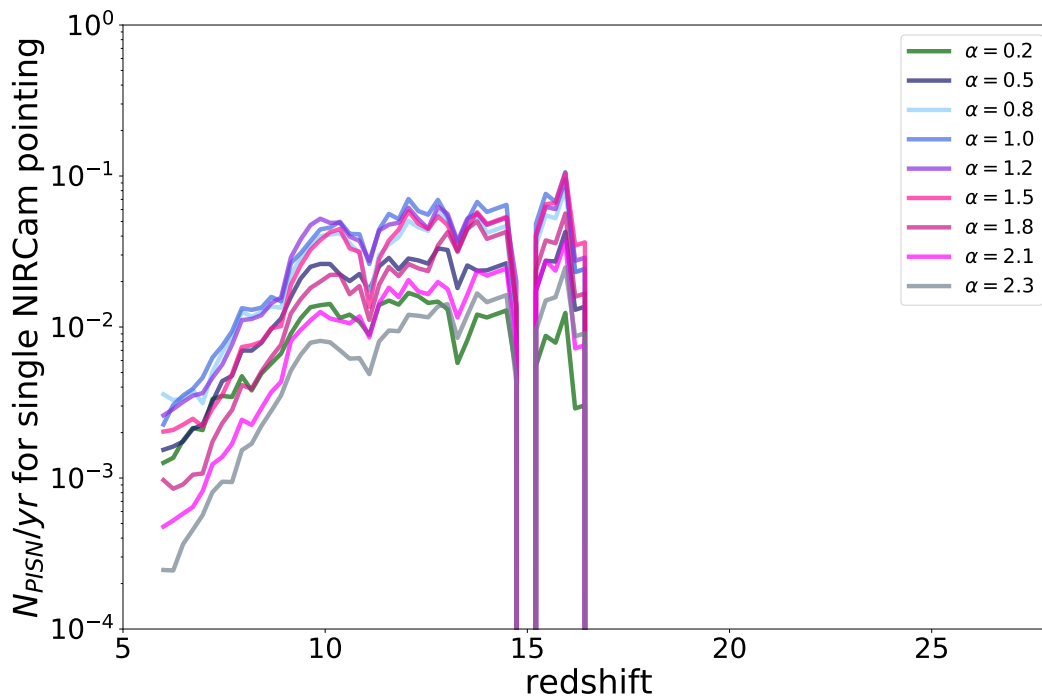


Figure 4.5: The PISN rate curves for each of our possible slopes of the IMF. The number of PISN per year for a single NIRCcam pointing of JWST is plotted as a function of redshift. The redshift range goes from $z=6$ to $z=30$. The curves are plotted for the case of a strong external Lyman-Werner with a maximum mass of a Pop III star at $8000 M_{\odot}$.

Although the number of PISN is the main focus of the project, to understand the reason for the turnaround, we look at the other potential fates of Pop III stars. In Figure 4.6, we plot the median number of Pop III stars in each halo that end their lives as CCSN ($M < 140 M_{\odot}$), PISN ($140 M_{\odot} < M < 260 M_{\odot}$) or DCBH ($M > 260 M_{\odot}$) versus the slope of the IMF (see Figure 1.4).

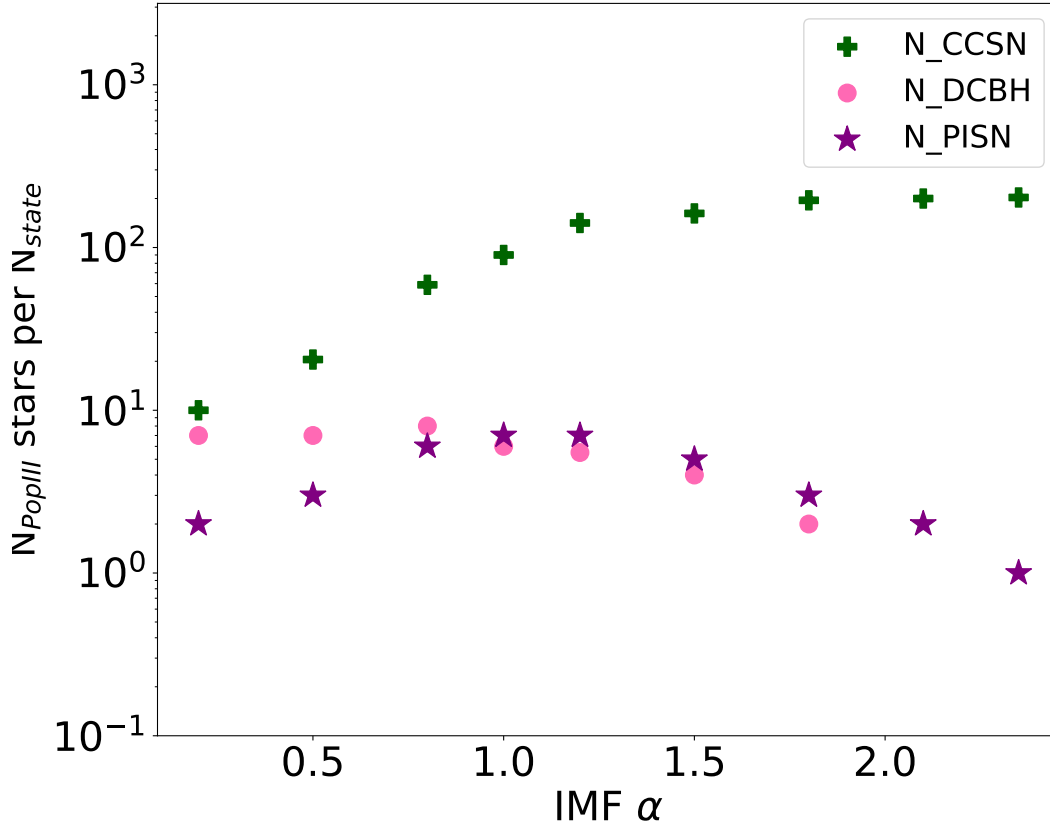


Figure 4.6: The median number of Pop III stars formed for each fate of the star as a function of the slope of the IMF. The slopes range from top heavy IMF ($\alpha = 0.2$) to bottom heavy IMF (Salpeter $\alpha = 2.35$). The plus sign represents the number of Pop III stars in the simulation that will end in a CCSN, a star sign is for stars exploding in PISN, and a circle sign for a DCBH fate). Note that this is for a low external Lyman-Werner case with a maximum mass of a Pop III star at $8000M_{\odot}$.

We notice the turnaround in the number of Pop III stars in the PISN mass range at a slope of $\alpha = 1.0$. As expected for the more bottom-heavy IMFs, the number of formed CCSN is much higher than that for PISN or DCBH, as the progenitor stars are less massive and more likely to form for these IMFs. However, at $\alpha < 1.0$ the median number of the most massive Pop III stars that end their lives as DCBHs has plateaued. This provides a critical clue for the reason for the turnaround in the number of PISN.

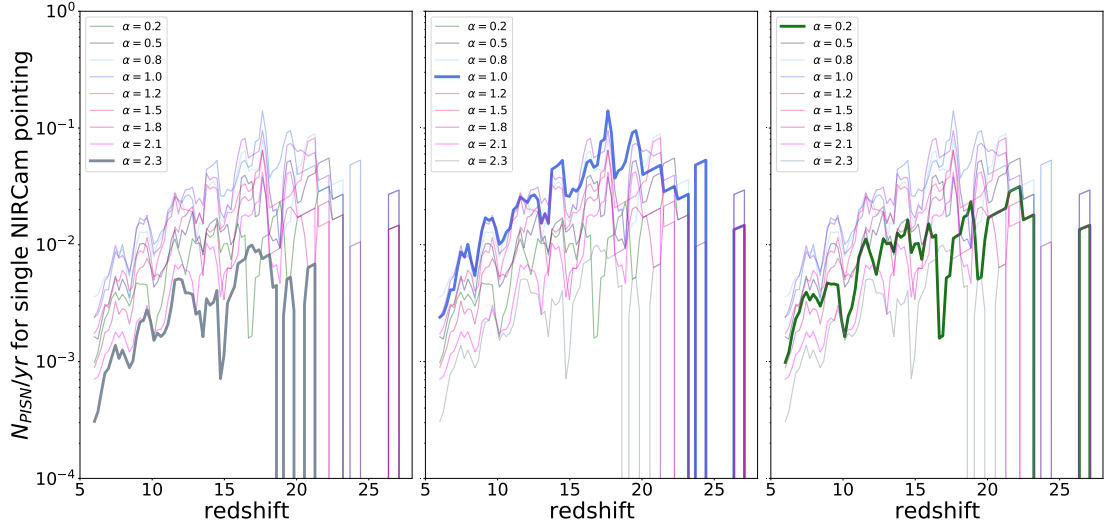


Figure 4.7: The rate of PISN per year for a single NIRCcam pointing as a function of redshift. All the curves shown here are plotted for a low external LW background, with a maximum mass of $8000 M_{\odot}$. The faded curves are identical in all three plots, but three main curves are shown in bold to highlight some differences in the rates at different IMF slopes. The leftmost plot accentuates the Salpeter slope ($\alpha = 2.35$), the middle plot highlights an IMF of ($\alpha = 1.0$), and the rightmost plot accentuates a very top-heavy IMF with a slope ($\alpha = 0.2$)

To highlight the turnaround, we select three curves for $m_{max} = 8000M_{\odot}$, $\alpha = 2.35$, $\alpha = 1.0$, and $\alpha = 0.2$ (Figure 4.7). We notice that the rates of PISN initially drop as we move towards a flatter IMF (center panel), before it decreases for the most top heavy IMFs (right panel). Since the mass of gas available for Pop III star formation is limited (Equation 3.2), if we form a few supermassive stars (e.g. $1000 M_{\odot}$), a large fraction of the available mass will be locked up in those stars, leaving us with less mass to form stars in the PISN range. Hence the PISN rates decrease again as in the rightmost plot of Figure 4.7. We repeat the above steps to plot the PISN rate curves for the case with a strong LW background and find the same result (Figure 4.8).

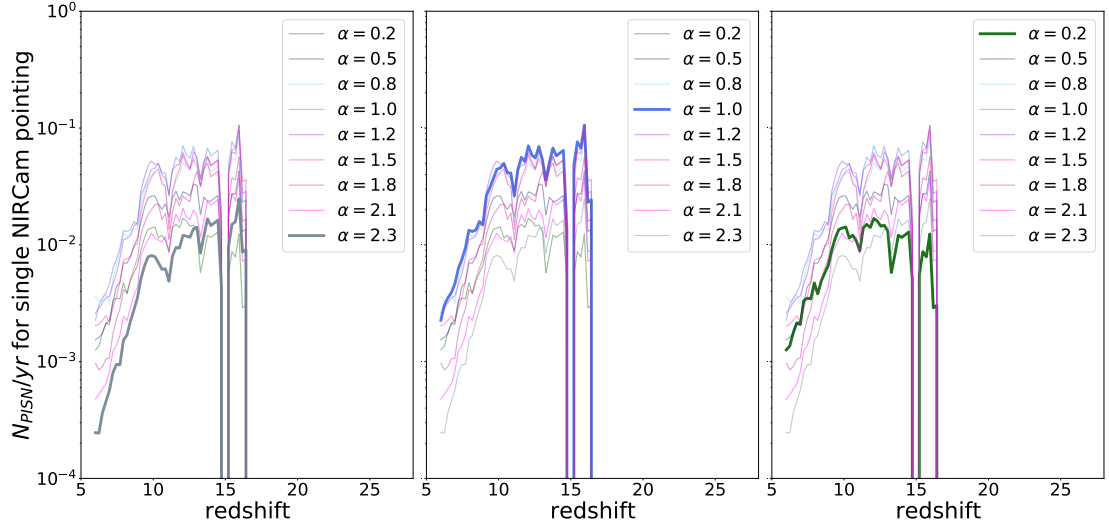


Figure 4.8: The rate of PISN per year for a single NIRCam pointing as a function of redshift. All the curves shown here are plotted for a high external LW background, with a maximum mass of $8000 M_{\odot}$. The faded curves are identical in all three plots, but three main curves are shown in bold to highlight some differences in the rates at different IMF slopes. The leftmost plot accentuates the Salpeter slope ($\alpha = 2.35$), the middle plot highlights an IMF of ($\alpha = 1.0$), and the rightmost plot accentuates a very top-heavy IMF with a slope ($\alpha = 0.2$)

4.1.1 Effect of the Maximum Pop III Mass

In addition to the slope of the Pop III IMF, the minimum and maximum masses of Pop III stars remains uncertain. Here we explore the dependence of our results on the maximum mass of a Pop III star.

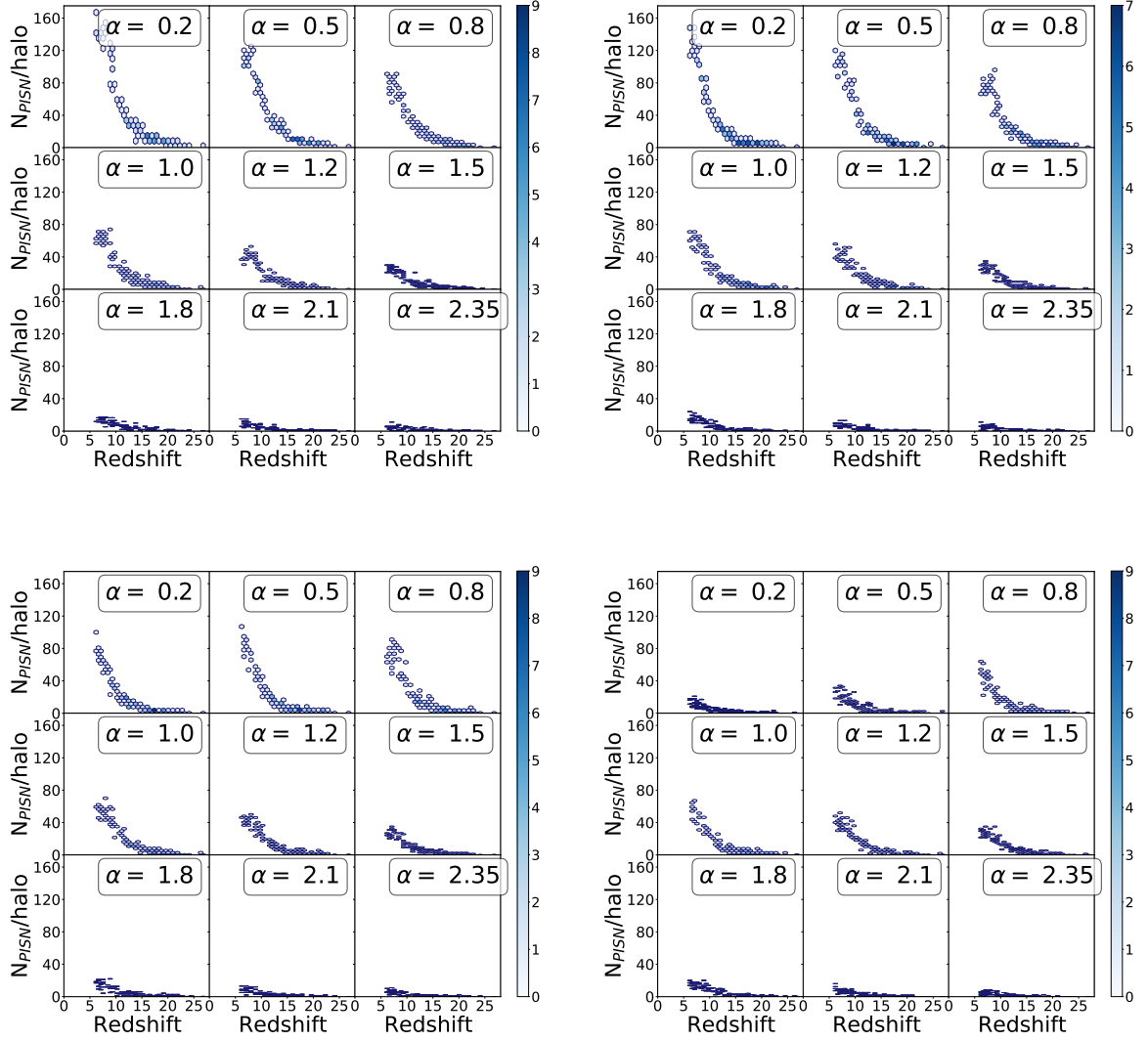


Figure 4.9: Heat maps of the number of PISN per halo as a function of redshift for four possible maximum masses of a forming Pop III stars. All maps represent a low external Lyman-Werner and are plotted for 9 different IMF slopes. The four tested maximum masses are $300 M_{\odot}$ (top left corner), $500 M_{\odot}$ (top right corner), $1000 M_{\odot}$ (bottom left corner), and $8000 M_{\odot}$ (bottom right corner)

We use a minimum mass of a Pop III star of $10 M_{\odot}$, in agreement with recipes from hydrodynamic simulations (Skinner & Wise 2020). However, we explore four values of the maximum mass, $m_{\text{max}} = [300 M_{\odot}, 500 M_{\odot}, 1000 M_{\odot}, 8000 M_{\odot}]$. In Figure 4.9 we show the heat maps of the number of PISN per halo per redshift across all slopes

of the IMF for all four m_{max} values. All runs shown here were done with the low LW background. The $m_{max} = 8000 M_{\odot}$ is the case discussed above. For $m_{max} = 1000 M_{\odot}$, we also see a turnaround in the number of PISN in a given halo, however the IMF slope at which it is occurring is more top-heavy ($\alpha = 0.5$) than in the $m_{max} = 8000 M_{\odot}$ case. However, the heat maps for the lowest m_{max} values (300 and 500 M_{\odot}) show the originally expected trend of the number of PISN increasing as the IMF slope decreases. This is what is expected if the turnaround in the number of PISN is due to increasing fractions of the mass available for Pop III star formation being locked up in a few extremely massive stars. As the maximum mass of a Pop III stars decreases, lower fractions of the mass available for Pop III star formation can be locked up in DCBHs.

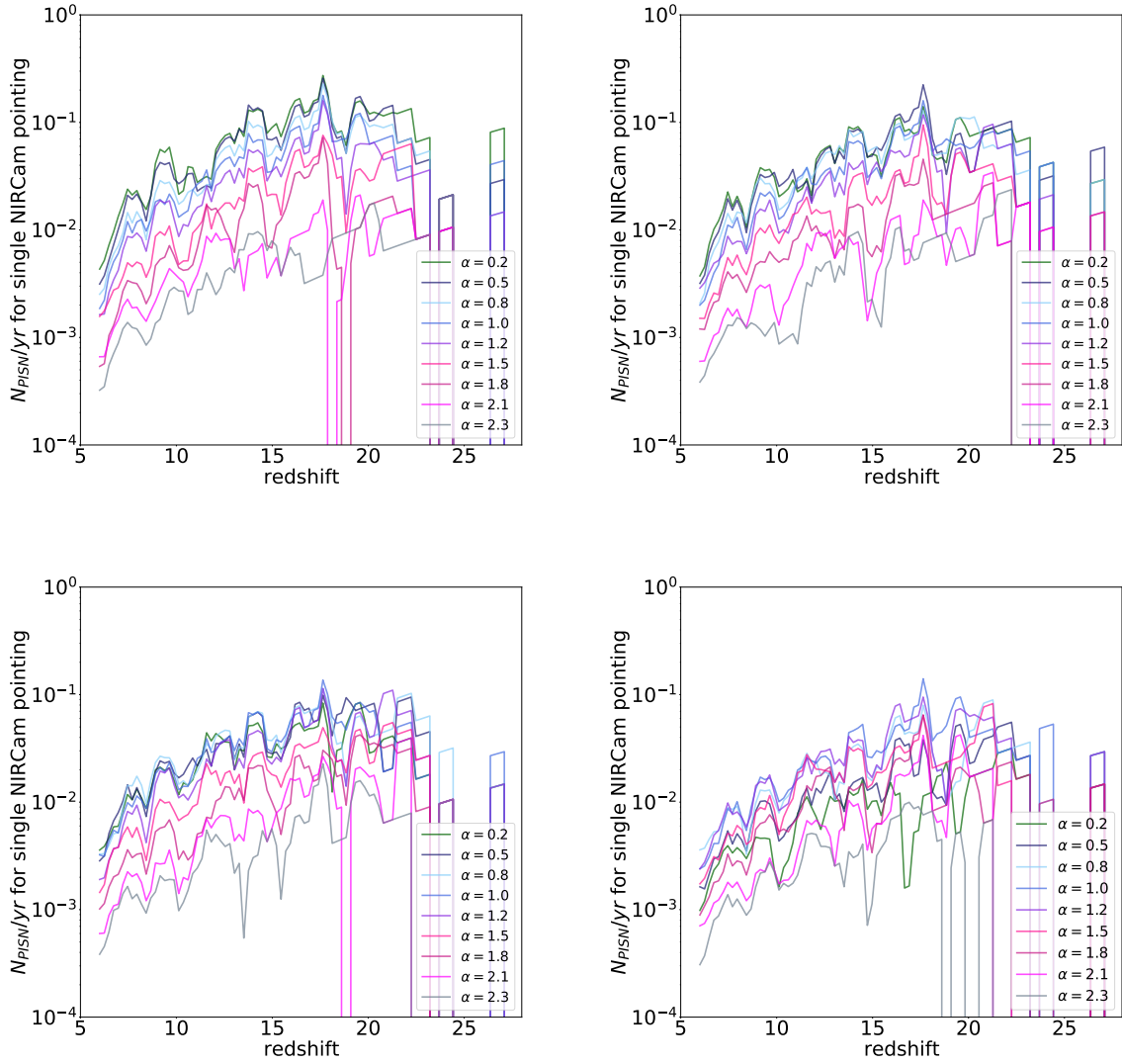


Figure 4.10: The number of PISN per year for a single NIRCcam pointing of JWST is plotted as a function of redshift for four different maximum masses of a Pop III star. The redshift range goes from $z=6$ to $z=30$ and the curves are plotted for the case with a low external Lyman-Werner. The four tested maximum masses are $300 M_{\odot}$ (top left corner), $500 M_{\odot}$ (top right corner), $1000 M_{\odot}$ (bottom left corner), and $8000 M_{\odot}$ (bottom right corner)

We now confirm that the dependence of the turnaround on m_{max} is also visible in the predicted rates of PISN. In Figure 4.10, we show the PISN rate plots for all four m_{max} values. To clarify this point, we reproduce Figure 4.6 for all possible Pop III maximum masses. Figure 4.11 shows the number of Pop III stars with a given fate. For all maximum masses, the number of DCBH seems to have dropped to near zero for $\alpha > 1.8$, due to the low chance of forming the most massive Pop III stars in more bottom-heavy IMFs.

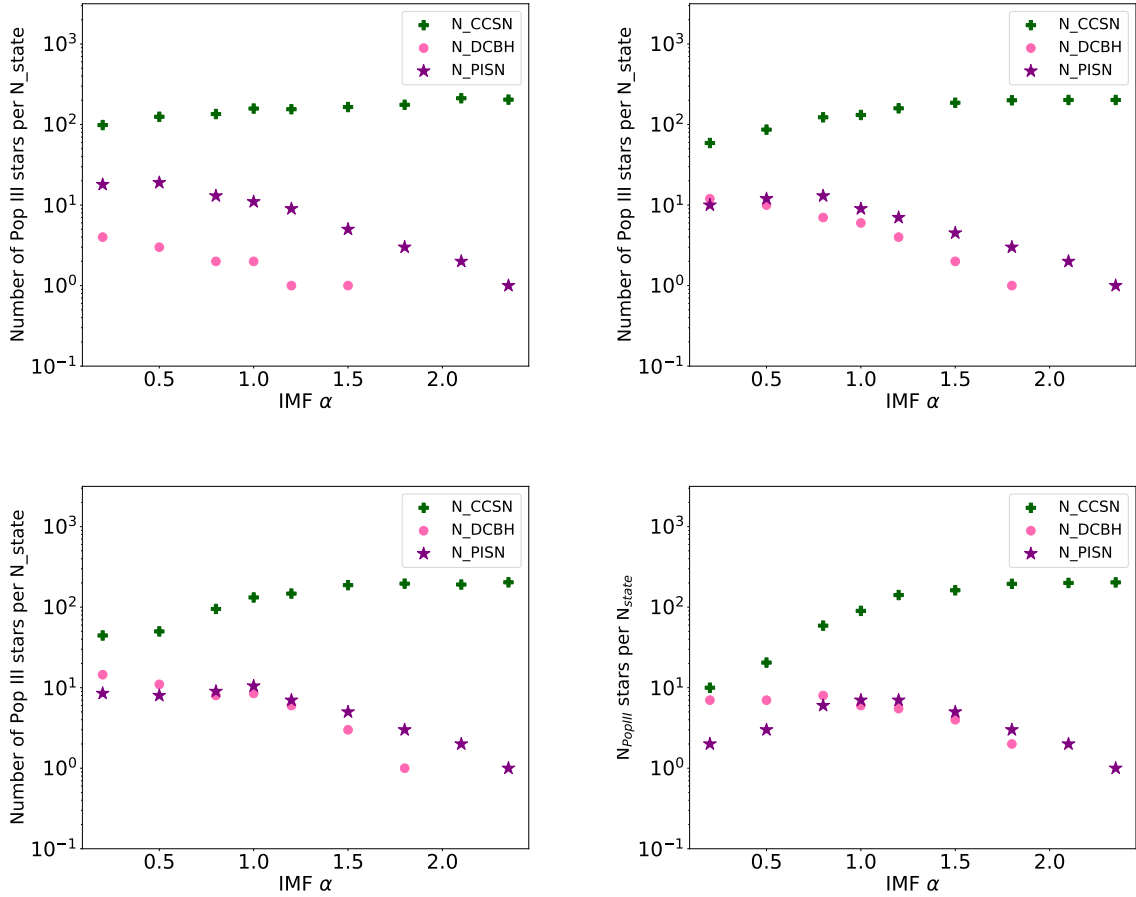


Figure 4.11: The number of Pop III stars formed for each fate of the star as a function of the slope of the IMF. The plus sign represents the number of Pop III stars in the simulation that will end in a CCSN, a star sign is for stars exploding in PISN, and a circle sign for a DCBH fate. Note that these plots are representative of a case with low external Lyman-Werner background and a varying maximum mass of a Pop III star. The four tested maximum masses are $300 M_{\odot}$ (top left corner), $500 M_{\odot}$ (top right corner), $1000 M_{\odot}$ (bottom left corner), and $8000 M_{\odot}$ (bottom right corner).

As the maximum mass decreases, the drop in the number of CCSN for the top-heavy IMFs also disappears, as there is more mass available to form stars in the CCSN mass range for lower m_{max} . Critically, we can see the moving of the turnaround to $\alpha \sim 0.5$ for $m_{max} = 1000M_{\odot}$ before disappearing entirely for m_{max} of $300 M_{\odot}$ and $500 M_{\odot}$. Finally we determine how the spread in the rate of PISN for our range of m_{max} compares to the spread due to the slope of the IMF. Figure 4.12 shows the rate of PISN for $\alpha = 2.35$, $\alpha = 1.0$, and $\alpha = 0.2$ for all four m_{max} values. We find that for more bottom-heavy IMFs ($\alpha = 1.0, \alpha = 2.35$) the difference in PISN rates for the IMF slopes is far greater than any difference due to the maximum Pop III stellar mass. It is only for the most top heavy IMF probed in this work ($\alpha = 0.2$), for which the change of PISN rate with varying m_{max} is comparable to the dependence on the IMF slope.

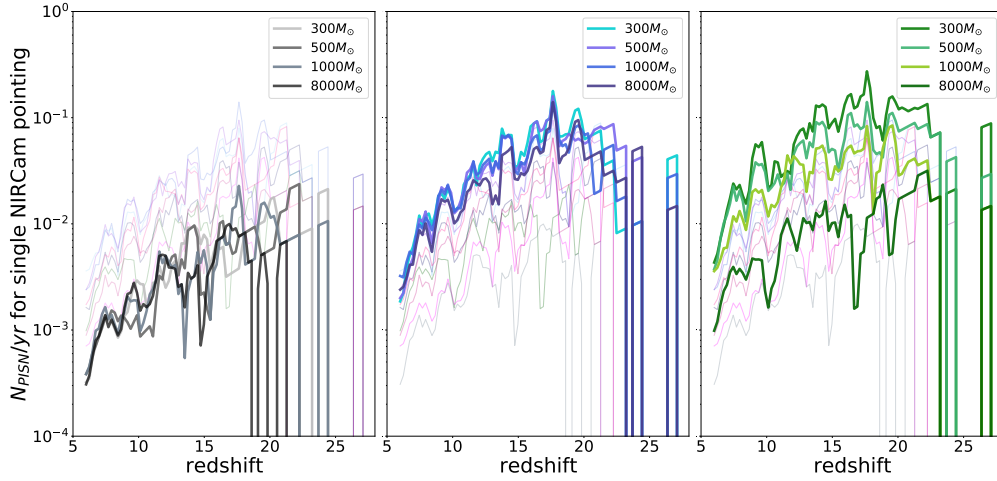


Figure 4.12: The rate of PISN per year for a single NIRCam pointing as a function of redshift. All the curves shown here are plotted for a low external LW background, with four possible maximum masses ($300 M_{\odot}$, $500 M_{\odot}$, $1000 M_{\odot}$, and $8000 M_{\odot}$). The faded curves are identical in all three plots (with $M_{max} = 8000 M_{\odot}$), but some curves are shown in bold to highlight some differences in the rates at different IMF slopes. Note that in each plot, we accentuate four curves of the same slope (one for each maximum mass). The leftmost plot accentuates four maximum masses with a Salpeter slope ($\alpha = 2.35$), the middle plot highlights an IMF of ($\alpha = 1.0$) for the four masses, and the rightmost plot accentuates a very top-heavy IMF with a slope ($\alpha = 0.2$) for four maximum masses.

Chapter 5

Discussion and Conclusion

5.1 Discussion

In Figure 5.1, we show the median number of Pop III stars in a given halo that will end up in a PISN state as a function of the IMF slope. The number of PISN is plotted for four different maximum mass limits ($300 M_{\odot}$, $500 M_{\odot}$, $1000 M_{\odot}$, and $8000 M_{\odot}$). The curves are plotted for both external LW backgrounds. Several of our key findings are summarized on this plot. We find, for a given external LW background, the median number of PISN per halo, and therefore the rate, is independent of m_{max} for bottom heavy IMFs. As stated in Chapter 4, this is due to the low probability of extremely massive Pop III stars forming for bottom heavy IMFs. As such, for $\alpha > 1.0$, large fractions of the primordial gas do not collapse into only a few extremely massive stars. For the top heavy IMFs ($\alpha < 1.0$), the median number of PISN per halo, and therefore the PISN rate, increases roughly linearly with decreasing m_{max} . The reason for this relatively linear relationship is unclear, and will be the subject of further investigation.

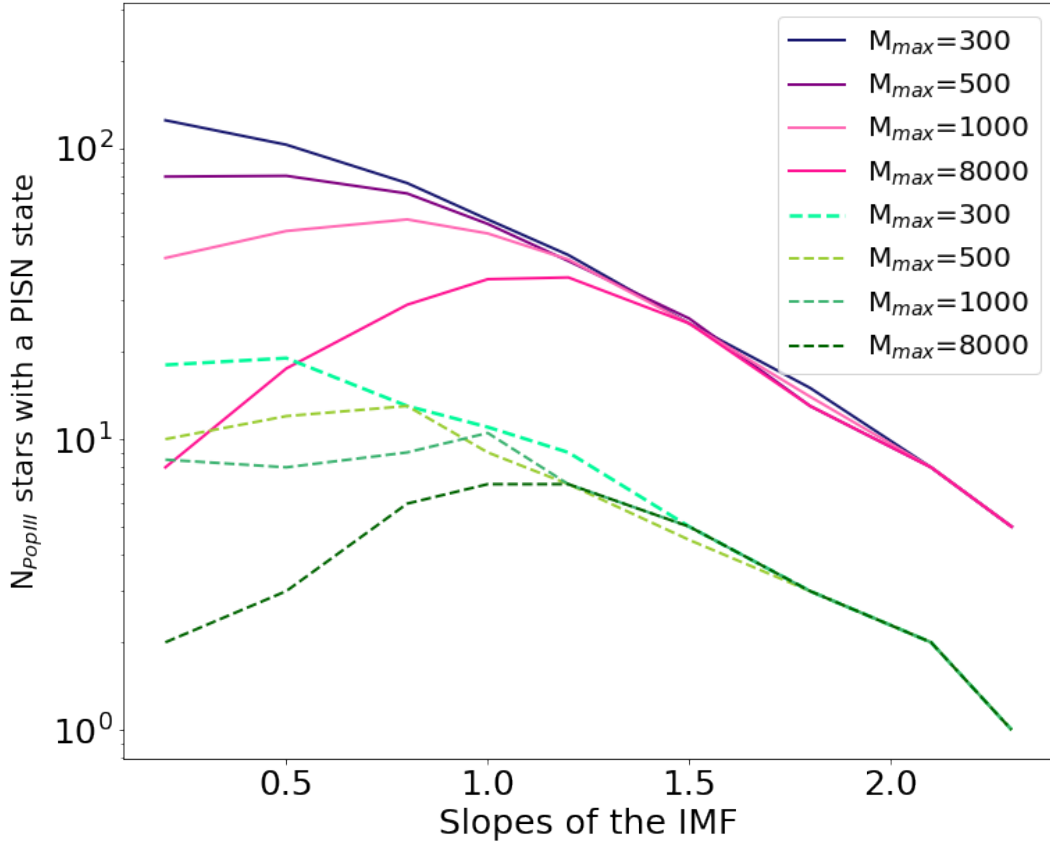


Figure 5.1: The number of Pop III stars that will explode as a PISN as a function of the IMF. The purple curves are plotted for a strong Lyman-Werner background, and the green curves reflect the number of PISN in a low LW background

While the dependencies of PISN rate on the IMF slope and m_{max} are independent of the strength of the LW background, the overall number of PISN and predictions for the observed rate do depend on the strength of the external LW background. The stronger the LW background, the greater the suppression of Pop III star formation in low mass halos, and the greater the amount of Pop III star formation occurring in more massive halos ($M_{vir} > 10^7 M_{\odot}$) at lower redshift ($z < 15$). We conclude that in the presence of a low LW, the smaller mass halos form Pop III stars at high redshift.

Enriched ejecta, largely from the PISN, proceed to pollute both their host halo, nearby halos and the surrounding IGM. As any halo that forms Pop III stars must be pristine, this eternal enrichment prevents their more massive descendants from forming Pop III stars. Conversely, in the presence of a strong LW background, star formation in small halos at high redshift is suppressed by the dissociation of H_2 , minimizing the enrichment processes described above. With a strong LW, massive halos that can self-shield their H_2 against the LW will remain pristine and form Pop III stars when they cross the mass threshold for cooling via HI . In addition to containing larger masses of gas, these halos will also undergo higher fragmentation (Equation 3.3), producing higher number of Pop III stars, and therefore higher numbers of PISN.

5.2 Conclusions

The conclusions of this work can be summarized as follows:

- The rate of PISN changes by an order of magnitude when the slope of a power Pop III IMF is varied. This suggests that observations of the PISN rate from JWST and the Roman Space Telescope will provide a power probe of mass distribution of Pop III stars.
- The PISN for top heavy ($\alpha < 1.0$) is linearly dependent on the maximum mass of a Pop III star. If the Pop III IMF was independently determined to be top heavy, the PISN is a potentially powerful probe of the maximum mass of Pop III stars.

- A stronger local LW background will suppress Pop III star formation in lower mass halos, decreasing the PISN rate at high redshifts $z > 15$, while increasing the PISN rate by as much as an order of magnitude at low redshifts ($z < 15$). This implies that to disentangle the effects of the LW background from the slope of the Pop III IMF will require observations of PISN rates from a range of redshifts.

Chapter 6

Future Work

There are various directions we can take this work. A selection of some of the more promising ones are below.

- Determine the dependence of the PISN rate on the remaining parameter of the mass distribution, m_{min} using a range of values drawn from recipes in hydrodynamic simulations.
- As seen in Figure 1.4, the minimum mass for hyper-luminous supernova might be $< 140M_{\odot}$. If we assume that all hyper-luminous supernova are PISN, we can explore the dependence of the PISN rate, as well as the enrichment of the IGM on the mass range of PISN.
- Explore the effect of a non-power law IMF, including exponential cut offs, and Gaussian distributions (Skinner & Wise 2020, Park et al. 2021b).

- Since PISN light curves are extremely bright in wavelengths other than the UV, incorporate emission from other rest frame wavelengths in our predictions for PISN rates for various JWST and Roman Space Telescope filters.

Appendix A

PISN Rate Calculations

In this appendix we present the details of the calculations we used to determine the PISN rates presented in Chapter 4. The following steps were done for all cases, however, for illustrative purposes we focus on a single case with a low external Lyman-Werner background, $\alpha = 1.0$, and $m_{max} = 1000M_{\odot}$. Figure A.1 shows our starting point of a heat map to show the number of halos with a given number of PISN throughout all redshifts in the simulation.

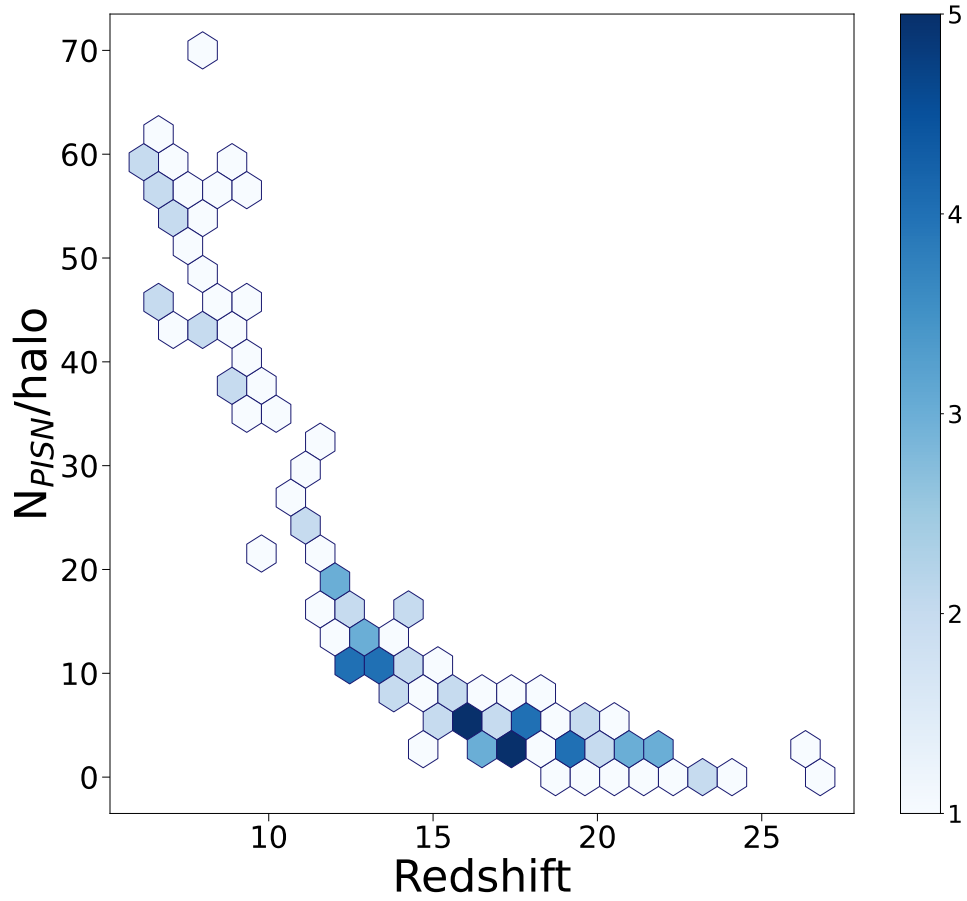


Figure A.1: Heat map of the number of PISN per each halo at a given redshift, for an IMF with slope $\alpha = 1.0$ and an $M_{max} = 1000M_{\odot}$. Each hexagon represents the number of halos with a given number of PISN at a given redshift. The darker the shade, the greater the quantity, and vice-versa.

The next step is to determine the total number of PISN which occur in all halos at a given redshift (Figure A.2).

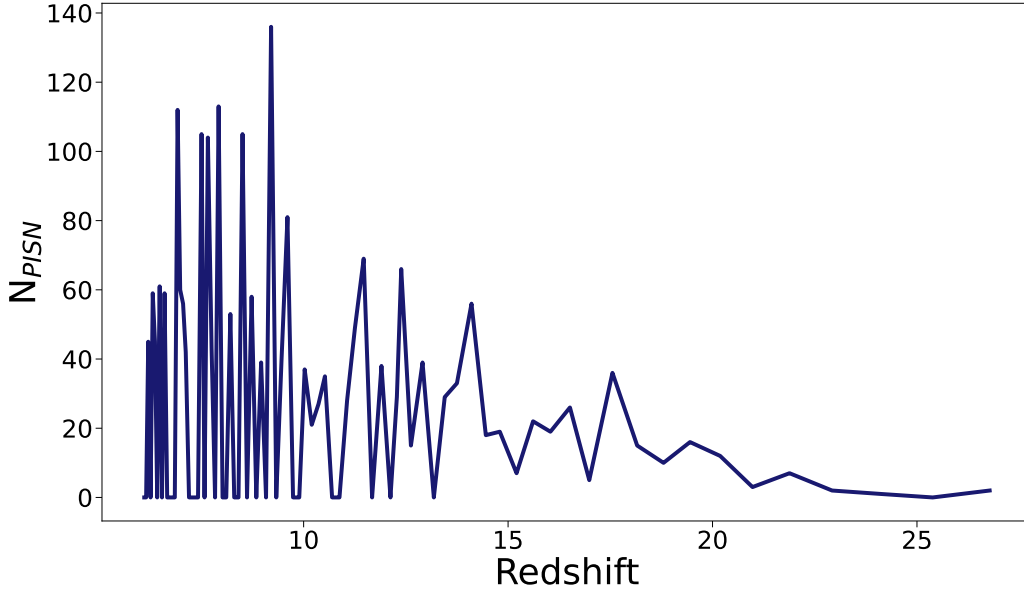


Figure A.2: Total number of PISN in all halos at each redshift for an IMF with a slope $\alpha = 1.0$.

Since we are making predictions for JWST, we look at the NIRC*am* filters in a bit more detail. The NIRC*am* filters on JWST have a finite width. Which, assuming that the SEDs of PISN peak in the UV and are redshifted in the NIRC*am* bands, translates to a range of PISN redshifts for which a given filter is sensitive. The wavelength range of a NIRC*am* filter ($\Delta\lambda_{NIRCam}$) corresponds to the change in redshift (Δz), and the wider the wavelength range, the larger the Δz . Therefore, to approximate the rates seen for a given redshift with NIRC*am* we must smooth our PISN over Δ_z . We choose $\Delta_z = 0.5$ to correspond to the wider NIRC*am* filters more suited to the deep and wide surveys required for PISN detection (Figure A.3).

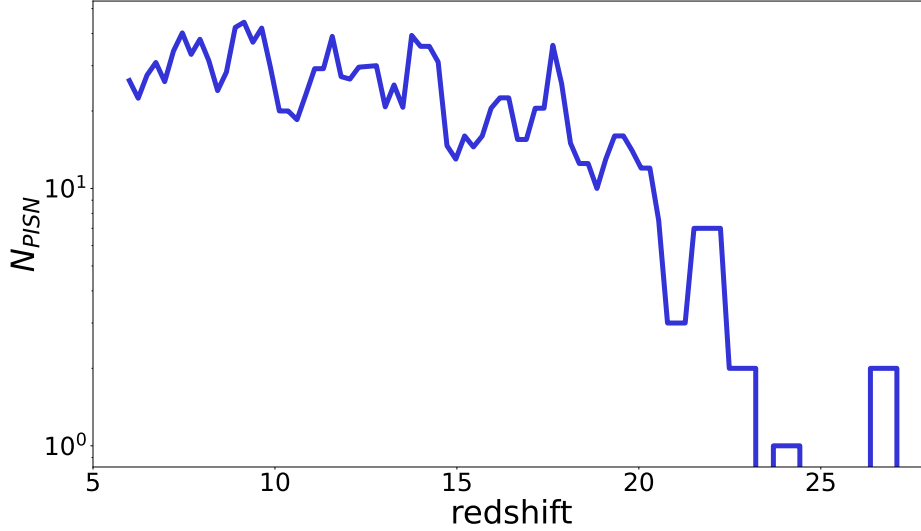


Figure A.3: The number of PISN per redshift for an IMF with slope $\alpha = 1.0$ and $M_{max} = 1000M_{\odot}$, after taking Δz into account. Note that we used $\Delta z = 0.5$ in our calculations.

We now have the number of PISN in our box at a given redshift smoothed over the width of the NIRCcam filter. Next, we need to determine the number of PISN that would be visible in a single NIRCcam pointing, which is $2.2' \times 2.2'$. To do this we need to determine the angular size of the box at a given redshift

$$\theta(z) = \frac{l_{box}(z)}{d_{comoving}(z)} \quad (\text{A.1})$$

where $l_{box}(z)$ is the physical size of the box at a given redshift z , $d_{comoving}$ is the comoving distance to an object at a given z and $\theta(z)$ is the angular size of the box in a side at a given z in radians. The physical box size is related to the comoving box size given in Chapter 2 by $l_{box}(z) = l_{cm}/(h(1 + z))$, where l_{cm} is the comoving box size, z is the redshift and h is the Hubble constant. It is now a simple matter to convert the angular

size of the box to arcminutes and calculate the number of NIRC*am* pointings, $N_{pointings}$ to cover the entire box as a function of redshift (Figure A.4). This is determined by dividing the angular size of the box in arcminutes by $2.2'$, giving us a number of PISN in a single NIRC*am* pointing, $N_{PISN_{NIRC\text{am}}} = N_{PISN} \times N_{pointing}^2$ (Figure A.5).

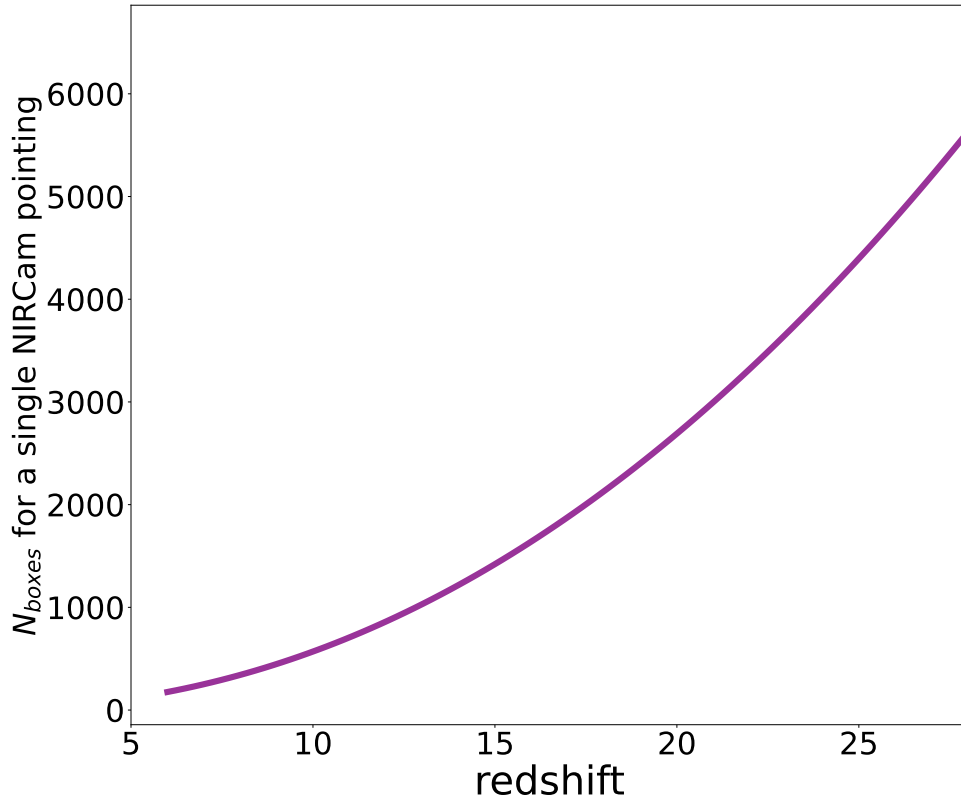


Figure A.4: Total number of boxes needed to make up a single NIRC*cam* pointing as a function of redshift.

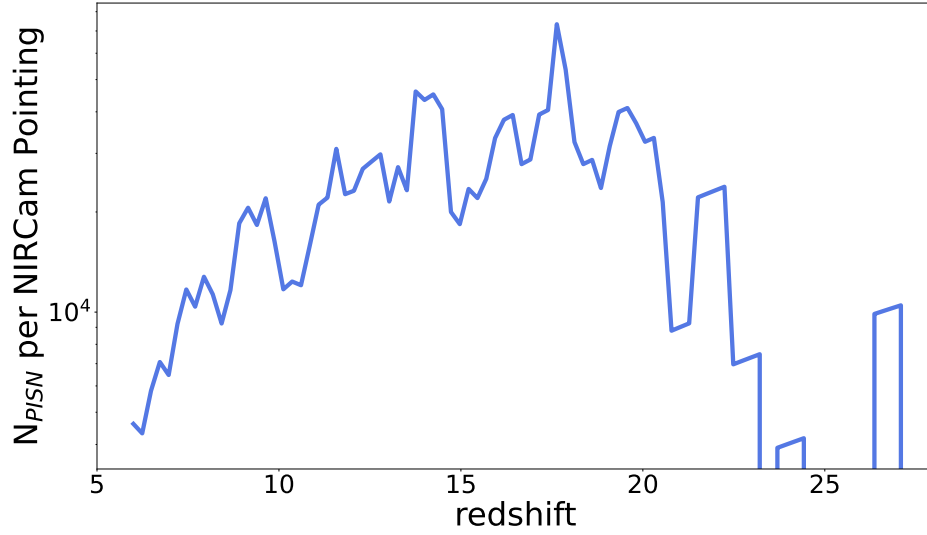


Figure A.5: The number of PISN per a single NIRCам pointing as a function of redshift.

Finally, we convert the number of PISN to the rate of PISN per in a single year. The Δt between snapshots is 10 Myr, the rate of PISN, $R_{PISN} = N_{PISN}/(\Delta t)$ (Figure A.6).

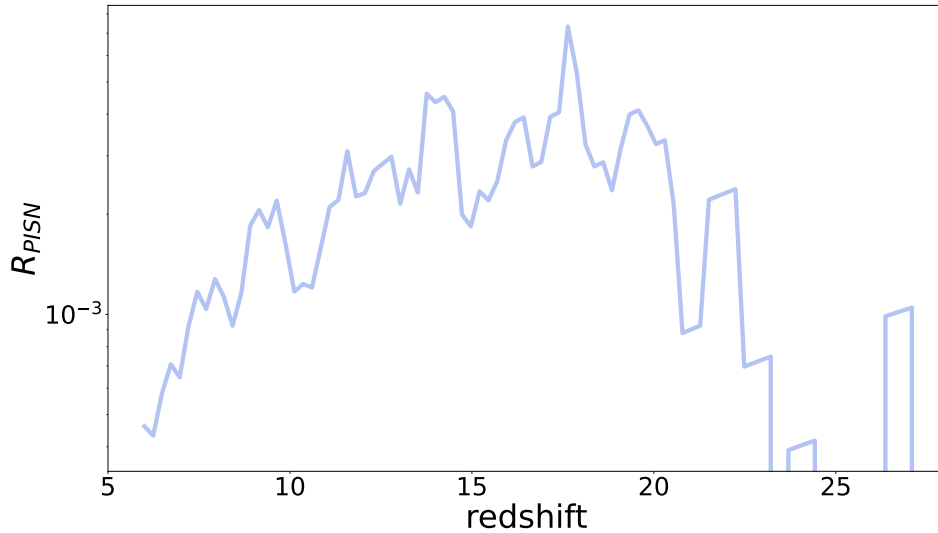


Figure A.6: Rate of PISN per year as a function of redshift.

The last step is to factor in the time dilation due to the expansion of space-time. The re-

lation between the R_{PISN} when the PISN explode and the observed rate today, $R_{PISN,cm}$ is:

$$R_{PISN_{cm}} = R_{PISN} * (1.0 + z) \quad (\text{A.2})$$

We can now plot the number of PISN per year expected to be observed in a single NIRCam pointing (Figure A.7).

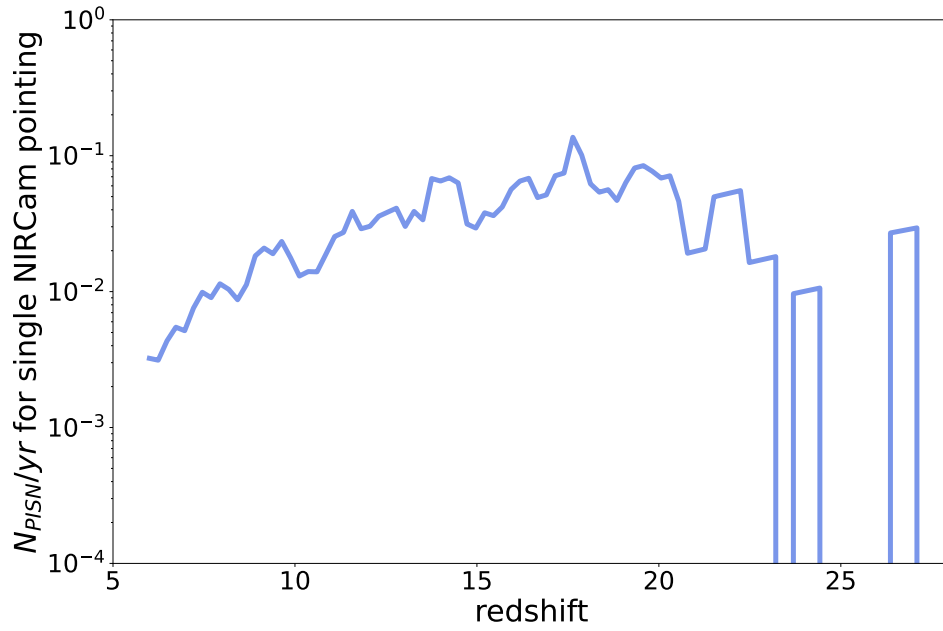


Figure A.7: Total number of PISN per year per redshift, for a single NIRCam pointing. The IMF used has a slope of $\alpha = 1.0$ and $M_{max} = 1000M_{\odot}$.

Bibliography

- Abel, T., Bryan, G. L., & Norman, M. L. 2002, *Science*, 295, 93
- Abel, T., Bryan, G. L., & Norman, M. L. 2002, *Science*, 295, 93
- Agarwal, B., Dalla Vecchia, C., Johnson, J. L., Khochfar, S., & Paardekooper, J.-P. 2014, *Monthly Notices of the Royal Astronomy Society*, 443, 648
- Behroozi, P. S., Wechsler, R. H., Wu, H.-Y., Busha, M. T., Klypin, A. A., & Primack, J. R. 2012, *The Astrophysical Journal*, 763, 18
- Fox, O. D., Baron, E., Bovill, M. S., Chen, T.-W., Filippenko, A. V., Foley, R., Ridden-Harper, R., Gezari, S., Gomez, S., Hook, I., Howell, A., Ibrahim, A., Kelly, P., Koekoemoer, A., Rubina, K., Mattila, S., Maund, J., Moriya, T., Perlmutter, S., Quimby, R., Pierel, J., Regos, E., Rest, A., Rubin, D., Stogler, L., Suzuki, N., Temim, T., Wang, Q., & Zenati, Y. 2021
- Gardner, J. P., Mather, J. C., Clampin, M., Doyon, R., Greenhouse, M. A., Hammel, H. B., Hutchings, J. B., Jakobsen, P., Lilly, S. J., Long, K. S., Lunine, J. I., McCaughrean, M. J., Mountain, M., Nella, J., Rieke, G. H., Rieke, M. J., Rix, H.-W., Smith, E. P., Sonneborn, G., Stiavelli, M., Stockman, H. S., Windhorst, R. A., & Wright, G. S. 2006, in *Society of Photo-Optical Instrumentation Engineers (SPIE) Conference Series*, Vol. 6265, *Society of Photo-Optical Instrumentation Engineers (SPIE) Conference Series*, ed. J. C. Mather, H. A. MacEwen, & M. W. M. de Graauw, 62650N
- Gill, S. P. D., Knebe, A., & Gibson, B. K. 2004, *Monthly Notices of the Royal Astronomical Society*, 351, 399
- Hahn, O. & Abel, T. 2011, *Monthly Notices of the Royal Astronomy Society*, 415, 2101
- Heger, A., Fryer, C. L., Woosley, S. E., Langer, N., & Hartmann, D. H. 2003, 591, 288
- Heger, A. & Woosley, S. E. 2002, *The Astrophysical Journal*, 567, 532
- Jaacks, J., Thompson, R., Finkelstein, S. L., & Bromm, V. 2018, *Monthly Notices of the Royal Astronomy Society*, 475, 4396
- Jaacks, J., Thompson, R., Finkelstein, S. L., & Bromm, V. 2018a, *Monthly Notices of the Royal Astronomical Society*, 475, 4396
- . 2018b, *Monthly Notices of the Royal Astronomical Society*, 475, 4396–4410

- Kasen, D., Woosley, S. E., & Heger, A. 2011, *The Astrophysical Journal*, 734, 102
- Knollmann, S. R. & Knebe, A. 2009, *The Astrophysical Journal Supplement Series*, 182, 608–624
- Maio, U., Dolag, K., Ciardi, B., & Tornatore, L. 2007, *Monthly Notices of the Royal Astronomy Society*, 379, 963
- Mezzacappa, A. & Messer, O. 1999, *Journal of Computational and Applied Mathematics*, 109, 281
- Park, J., Ricotti, M., & Sugimura, K. 2021a, *Monthly Notices of the Royal Astronomy Society*
- . 2021b, *Monthly Notices of the Royal Astronomy Society*
- Ricotti, M., Parry, O. H., & Gnedin, N. Y. 2016, *The Astrophysical Journal*, 831, 204
- Salpeter, E. E. 1955, *The Astrophysical Journal*, 121, 161
- Skinner, D. & Wise, J. H. 2020, *Monthly Notices of the Royal Astronomical Society*, 492, 4386–4397
- Springel, V. 2005, *Monthly Notices of the Royal Astronomy Society*, 364, 1105
- Stiavelli, M. 2009, *From First Light to Reionization: The End of the Dark Ages*
- Susa, H., Hasegawa, K., & Tominaga, N. 2014, *The Astrophysical Journal*, 792, 32
- Trenti, M. & Stiavelli, M. 2009, *The Astrophysical Journal*, 694, 879
- Wagoner, R. V. 1969, *The Annual Review of Astronomy and Astrophysics*, 7, 553
- Weinmann, S. M. & Lilly, S. J. 2005, 624, 526
- Whalen, D. J., Fryer, C. L., Holz, D. E., Heger, A., Woosley, S. E., Stiavelli, M., Even, W., & Frey, L. H. 2013, *The Astrophysical Journal Letters*, 762, L6
- Windhorst, R. A., Timmes, F. X., Wyithe, J. S. B., Alpaslan, M., Andrews, S. K., Coe, D., Diego, J. M., Dijkstra, M., Driver, S. P., Kelly, P. L., & Kim, D. 2018, *Astrophysical Journal Supplement*, 234, 41
- Wise, J. H., Turk, M. J., Norman, M. L., & Abel, T. 2012, *The Astrophysical Journal*, 745, 50

VITA

Personal Background	Alessa Ibrahim Wiggins Damascus, Syria Daughter of Wissam Ibrahim and Ghedaa Issa
Education	Diploma, Al Maouneh High School, Damascus, Syria, 2014 Bachelor of Arts, Physics, California State University, San Bernardino, CA, 2019
Experience	Summer Internship, California State University, San Bernardino, CA, 2017 Summer Internship, Stanford University, Stanford, CA, 2018 Teaching Assistantship, Texas Christian University, Fort Worth, 2019-2021
Professional Memberships	American Astronomical Society

ABSTRACT

DEPENDENCE OF THE PREDICTED PAIR-INSTABILITY SUPERNOVA RATE ON THE POP III INITIAL MASS FUNCTION

by Alessa Ibrahim Wiggins, MSc., 2021
Department of Physics and Astronomy
Texas Christian University

Mia S. Bovill Assistant Professor of Physics

Population III stars are a theoretical population of metal-free stars which formed during the first billion years after the Big Bang and ended the Cosmic Dark Ages. However, to date, Pop III stars have not been directly observed, as such our knowledge of this population is dependent on theoretical work. Upcoming observations provide us with the first opportunity to detect Pop III stars and their effects. This work focuses on the subset of Pop III stars that end in hyper-luminous Pair Instability Supernovae (PISN), which are within reach of direct detection by JWST. Coupling observed PISN rates to the astrophysics of the first stars requires a quantitative understanding of the dependence of PISN rates on the Pop III stellar initial mass function (IMF). We present results from a new semi-analytic model (SAM) which treats the slope of the Pop III IMF and the maximum mass of Pop III stars as free parameters.